A direct Arbitrary-Lagrangian-Eulerian finite volume scheme on nonconforming moving unstructured meshes: logically straight slip-lines

Elena Gaburro[a], Michael Dumbser*[b]

[a]*Department of Mathematics, University of Trento, Via Sommarive, 14 - 38123 Trento, Italy*
[b]*Department of Civil, Environmental and Mechanical Engineering, University of Trento, Via Mesiano, 77 - 38123 Trento, Italy.*

arXiv:1602.01703v1 [math.NA] 4 Feb 2016

Abstract

In this paper, we present a novel second-order accurate Arbitrary-Lagrangian-Eulerian (ALE) finite volume scheme on *nonconforming* polygonal grids, in order to avoid the typical mesh distortion caused by *shear flows* in Lagrangian-type methods. In our new approach the nonconforming element interfaces are *not* defined *a priori* by the user, but they are automatically detected by the algorithm, if the tangential velocity difference across an element interface is sufficiently large. The new scheme then subdivides the neighbors into two groups, each of which has similar properties, namely the *left* and the *right* neighbors. The nodes far away from the shear discontinuity are moved with a standard node solver, while for those at the interface a *new node* is inserted in such a way that the old one moves according to an averaged velocity over the left neighbors, and the new one slides along the edge according to the average velocity prescribed by the right group.

The core of the proposed method is the *local* update of all the necessary connectivity tables, as a consequence of the insertion or the deletion of nodes and edges, and the computation of the numerical fluxes between the space-time control volumes, taking in particular into account that the lateral faces can be shared between more than two elements. The final ALE finite volume scheme is based directly on a space-time conservation formulation of the governing PDE system, which completely avoids the need of an additional remapping stage, hence the new method is a so-called *direct* ALE scheme. Second order of accuracy in space and time is obtained by using a MUSCL-Hancock strategy, together with a Barth and Jespersen slope limiter and a time-evolution of the reconstruction polynomials to the space-time midpoints of each moving control volume and of each part of the space-time lateral surfaces. Due to the space-time conservation formulation of our algorithm, the geometric conservation law (GCL) is *automatically* satisfied by *construction*, moreover the mesh quality remains high and, as a direct consequence, also the time step remains almost constant in time, even for highly sheared vortex flows. Up to now we are able to maintain logically straight slip-line interfaces.

A large set of different numerical tests has been carried out in order to check the accuracy and the robustness of the new method for both smooth and discontinuous problems. In particular we have compared the results for a steady vortex in equilibrium solved with a standard *conforming* ALE method (without any rezoning technique) and with our new *nonconforming* ALE scheme, to show that the new nonconforming scheme is able to avoid mesh distortion even after very long simulation times.

Key words: moving unstructured nonconforming mesh, slide lines, direct Arbitrary-Lagrangian-Eulerian (ALE) methods for shear flows, cell-centered Lagrangian Godunov-type finite volume methods, shallow water equations in Cartesian and cylindrical coordinates, hyperbolic conservation laws.

*Corresponding author
Email addresses: elena.gaburro@unitn.it (Elena Gaburro), michael.dumbser@unitn.it (Michael Dumbser*)

1. Introduction

Arbitrary-Lagrangian-Eulerian (ALE) finite volume schemes are characterized by a moving computational mesh: at each time step the new position of all the nodes has to be recomputed according to a prescribed mesh velocity, which generally is chosen as close as possible to the local fluid velocity (as it is in the pure Lagrangian framework), but it can also be set to zero (to reproduce the Eulerian case), or it can be chosen arbitrarily. The aim of these methods is to reduce the numerical dissipation errors due to the convective terms, hence to capture contact discontinuities sharply and to precisely identify and track material interfaces. For these reasons already in the 1950ies John von Neumann and Richtmyer were working on Lagrangian schemes [59] for one-dimensional flows, and Wilkins proposed a two-dimensional extension in 1964, see [60].

Since the fluid velocity is required at each node and at each time step, the most natural approach is a *staggered* discretization, where the momentum is defined at the grid vertices and all the other flow variables are defined at the cell center. Despite some drawbacks of the initial version of staggered Lagrangian schemes, which was not conservative and which produced some spurious modes in the numerical solution, it was widely used in the last forty years and many improvements have been made in the meantime; for further details one can refer to the papers of Caramana and Shashkov [16, 17] and of Loubère at al. [46, 47]. Moreover, examples of optimal results on general polygonal grids have been presented in [49].

An alternative consists in a *conservative cell-centered* discretization, which was first introduced by Godunov in [37, 38]. An early application of conservative cell-centered Godunov-type schemes to the compressible Euler equations of gas dynamics in a Lagrangian framework on moving grids was provided by Munz in [54], using Roe-type and HLL-type approximate Riemann solvers. In many recent papers, see for example Carré et al. [18, 53], Després et al. [25, 26], Maire [50, 51, 52] and Yu at al. [43], the conservative cell-centered Godunov-type approach is used both with structured and unstructured moving grids and in two and three space dimensions, respectively.

Successively also better than second-order accurate schemes were introduced: *high order* of accuracy in *space* was first achieved by Cheng and Shu [20, 21] by means of a nonlinear ENO reconstruction, and high order in *time* was obtained either by the use of Runge-Kutta type methods or by adapting the ADER-WENO schemes to the Lagrangian framework, see for example Dumbser et al. [33] and Cheng & Toro [22]. Recent work on high order Lagrangian discontinuous Galerkin finite element methods can be found in the papers of Vilar et al. [36, 34, 35], while high order Lagrangian continuous finite elements have been studied by Scovazzi et al. [55, 56] and Dobrev and Rieben et al. [27, 28, 29].

For all the cell-centered methods an important step is the computation of the fluid velocity at the nodes, since this information is not directly available in the scheme, but it has to be extrapolated from the adjacent cells. To obtain these values three different types of *node solvers* can be employed. The simplest one is that proposed in the above mentioned papers by Cheng and Shu [20, 44], somehow employed also in this work, where the node velocity is obtained as arithmetic average among the near states; another possibility, suggested by Després et al. (GLACE scheme) [18] and Maire (EUCCLHYD scheme) [50], is to solve multiple one-dimensional half-Riemann problems around a vertex, in order to get an approximate solution of the multi-dimensional (generalized) Riemann problem at the node; the most recent method introduced by Balsara et al. [1, 30, 2, 3] consists in solving approximately a multidimensional Riemann problem at the nodes, using a new family of genuinely multidimensional HLL-type Riemann solvers. They are all compared with each other within a high-order ADER-WENO ALE scheme in the recent paper of Boscheri et al. [11].

Although all these different schemes are widely used, especially to describe compressible multi-material flows, a common problem that affects all Lagrangian methods is the severe mesh *distortion* or the mesh tangling that happens in the presence of shear flows and that may even destroy the computation. Hence, all Lagrangian methods must be in general combined with an algorithm to (locally) rezone the mesh at least from time to time and to remap the solution from the old mesh to the new mesh in a conservative manner. Lagrangian remesh and remap ALE schemes are very popular and some recent work on that topic can be found in [6, 7, 14, 41, 61]. Extensions of the remesh-remap approach to better than second-order of accuracy

can be found in [45, 48, 19]. In contrast to indirect ALE schemes (purely Lagrangian phase, remesh and subsequent remap phase) there are the so-called direct ALE schemes, where the local rezoning is performed before the computation of the numerical fluxes, hence changing directly the chosen mesh velocity of the ALE approach, see for example [8, 9, 10] for recent work in that direction based on high order ADER-WENO schemes.

Moreover in realistic application, when dealing with shear flows at material interfaces (for example in a high velocity impact problem [40]) or generally in any Lagrangian hydrocode that allows different materials or regions to move relative to each other with different velocities and for a long time, a *slide lines* treatment is required. The introduction of slide lines goes back to an idea of Wilkins [60], successively studied and refined by Caramana [15], Barlow et al. [4] and Loubére at al. [42]; the main ideas adopted in their papers regard the subdivision of the nodes at the interface in master and slave nodes and the study of the forces between the two sides of the slide lines. Another very interesting approach to slide lines was presented by Clair et al. in [23, 24]. In [16] a staggered Lagrangian code has been presented, where the internal interfaces are handled with a special type of boundary condition.

This paper presents a novel second-order accurate *direct* cell-centered ALE scheme on unstructured polygonal grids, which deals with shear flows in an original and effective way. The sliding element interfaces are automatically *detected* during the computation (not fixed *a priori*), and nodes along such sliding edges are allowed to move in a *nonconforming* way by the insertion and deletion of new nodes and new edges. The algorithm can handle both the insertion and the deletion of nodes and edges, using completely *local* procedures. In the straight slip-line case no distinction between master and slave nodes is required and the mesh movement is only based on the corner-extrapolated values of the fluid velocity, eventually projected onto the nearest edge to avoid the creation of holes or the superposition of elements.

At this point we also would like to refer to some recent work on high order Eulerian and ALE schemes on moving meshes with time-accurate *local time stepping* (LTS) presented in [31, 13, 39], where each element is allowed to run at its own optimal local time step according to a *local* CFL stability condition. The resulting algorithms use a *conforming* grid in space, but naturally produce a *nonconforming* mesh in time. Therefore, the new nonconforming ALE method presented in this paper, which produces a nonconforming mesh in both space and time, is naturally related to some of the ideas forwarded in [31, 13] in the context of local time stepping.

The rest of the paper is organized as follows. At the beginning of Section 2 we outline the main stages of the proposed numerical method, then we describe the employed second order finite volume scheme emphasizing the novelties due to the non conforming mesh motion. In particular in Section 2.5 we explain how to deal with the moving nonconforming (hanging) nodes and the corresponding *local* update of the connectivity tables of the unstructured mesh. In Section 3 some numerical test problems are presented in order to check the efficiency and the robustness of the proposed approach in maintaining straight slip-lines, a high quality mesh, local and global volume conservation, and in satisfying the GCL condition. The paper is closed by an outlook to future extensions concerning the high-order case and to more general piece-wise linear slide lines.

2. Numerical method

We consider two-dimensional non linear hyperbolic systems of conservation laws that can be cast in the following general form

$$\frac{\partial \mathbf{Q}}{\partial t} + \nabla \cdot \mathbf{F}(\mathbf{Q}) = \mathbf{S}(\mathbf{Q}), \quad \mathbf{x} \in \Omega(t) \subset \mathbb{R}^2, \mathbf{Q} \in \Omega_{\mathbf{Q}} \subset \mathbb{R}^{\nu}, \tag{1}$$

where $\mathbf{x} = (x, y)$ is the spatial position vector, t represents the time, $\mathbf{Q} = (q_1, q_2, \ldots, q_{\nu})$ is the vector of conserved variables defined in the space of the admissible states $\Omega_{\mathbf{Q}} \subset \mathbb{R}^{\nu}$, $\mathbf{F}(\mathbf{Q}) = (\,\mathbf{f}(\mathbf{Q}), \mathbf{g}(\mathbf{Q})\,)$ is the non linear flux tensor, and $\mathbf{S}(\mathbf{Q})$ represents a non linear algebraic source term.

To discretize the moving domain, we consider a total number N_E of polygonal elements T_i^n (the *spatial control volumes*), each one with an arbitrary number of vertices $N\mathrm{v}(i)$, $i = 1, \ldots, N_E$: the union of all these elements results in an unstructured mesh $\mathcal{T}_\Omega^n$ which covers the computational domain $\Omega(\mathbf{x}, t^n) = \Omega^n$ at the current time t^n and which contains a total number N_{node}^n of nodes and a total number N_{edge}^n of edges.

At each time step the algorithm evolves the cell averages via a discrete form of the equation (1) and computes the new node positions through the following intermediate stages:

I. First, the edges along relevant shear flows are detected and the nodes on these edges are marked as problematic.
II. Then the new node positions are computed according to the type of the considered node, in particular
   a) regular non-hanging nodes that are not in regions of relevant shear flow (i.e. they have not been marked as problematic) are evolved using a mass-weighted Cheng and Shu node solver;
   b) regular non-hanging nodes that are in regions of relevant shear flow (i.e. they have been marked as problematic) are *doubled*; their new position is projected along the nearest interface edge, and they subsequently change their type from regular non-hanging nodes to *hanging* nodes;
   c) hanging nodes on an edge are allowed to slide only along that edge, and if they get too close to other nodes, they are *merged* together (deleted), eventually changing back their type from hanging nodes to regular non-hanging nodes.
III. Finally, we apply a MUSCL-Hancock strategy to produce a space-time reconstruction of the data from the known cell averages, and to evolve the solution to the new geometry (without any remapping stage) using a space-time conservation formulation of the governing PDE system.

While this is the natural execution order in the computer program, for the sake of clarity we first start this section by briefly summarizing our space-time finite volume scheme, focusing in particular on the computation of the *numerical fluxes* at the *nonconforming interfaces*. Only later, after having introduced the connectivity tables employed in the algorithm (Section 2.3) and having described the interface detector (Section 2.4), we will discuss in detail the procedure how to move each kind of node and the corresponding *local* update of the connectivity tables.

2.1. Finite volume scheme: reconstruction and time-evolution

As usual in a classical cell-centered finite volume scheme, at the beginning of each time step t^n we dispose of the cell averages $\mathbf{Q}_i^n$ of the conserved variables for each spatial control volume T_i^n , defined as

$$\mathbf{Q}_i^n = \frac{1}{|T_i^n|} \int_{T_i^n} \mathbf{Q}(\mathbf{x}, t^n)\, d\mathbf{x},$$

where $|T_i^n|$ denotes the area of T_i^n. These are the data computed and stored at the previous time, and which will be used to evolve the solution during the current time step. To construct a method which is better than first order accurate we cannot compute the numerical fluxes directly with these piecewise constant data, but we have to reconstruct for each T_i^n a piecewise space-time polynomial $\mathbf{q}_h(\mathbf{x}, t^n)$, exploiting the cell averages of the cell and its neighbors, combined with a time-evolution procedure.

Here, second order of accuracy in space and time is achieved by using the MUSCL-Hancock strategy that was for the first time proposed by van Leer in [58] and which is very well explained in [57], slightly adapted to our context of a nonconforming moving mesh.

For the *spatial* reconstruction, let us define a polynomial $\mathbf{w}_h(\mathbf{x}, t^n)$ of the form

$$\mathbf{w}_h(\mathbf{x}, t^n)\,|_{T_i^n} = \mathbf{Q}_i^n + \nabla \mathbf{Q}_i(\mathbf{x} - \mathbf{x}_i), \qquad \mathbf{x} \in T_i^n,$$

where $\mathbf{x}_i$ is the barycenter of cell T_i^n. We denote with $\mathcal{S}_i^n$ the set of neighbors of T_i^n that share a common edge with T_i^n (the set $\mathcal{S}_i^n$ may change at each time step). To compute ∇Q_i, integral conservation is imposed on each element of $\mathcal{S}_i^n$

$$\frac{1}{|T_j^n|} \int_{T_j^n} \mathbf{w}_h(\mathbf{x}, t)\, d\mathbf{x} = Q_j^n \quad \forall T_j^n \in \mathcal{S}_i^n. \tag{2}$$

The above system is in general over-determined, so we add the constraint that equation (2) holds exactly at least for T_i^n. This is easily satisfied by rewriting the equations as

$$\frac{1}{|T_j^n|}\int_{T_j^n} \nabla\mathbf{Q}_i(\mathbf{x}-\mathbf{x}_i)\,d\mathbf{x} = Q_j^n - Q_i^n \quad \forall T_j^n \in \mathcal{S}_i^n, \tag{3}$$

then we solve (3) via a classical least-squares approach using the normal equation of (3), and we thus obtain the *non-limited* slope $\nabla\mathbf{Q}_i$.

To ensure that new extrema are not created in the reconstruction process, we employ the *slope limiter* presented by Barth and Jespersen in [5]. The idea is to find the largest admissible Φ_i in such a way that

$$\tilde{\mathbf{w}}_h(\mathbf{x},t^n) = \mathbf{Q}_i^n + \Phi_i\nabla\mathbf{Q}_i(\mathbf{x}-\mathbf{x}_i)$$

satisfies

$$\min_{j\in\mathcal{V}_i^n}\mathbf{Q}_j^n = \mathbf{Q}_i^{min} \le \tilde{\mathbf{w}}_h(\mathbf{x},t^n) \le \mathbf{Q}_i^{max} = \max_{j\in\mathcal{V}_i^n}\mathbf{Q}_j^n,$$

where $\mathbf{Q}_i^{max}$ and $\mathbf{Q}_i^{min}$ are the componentwise maximum and minimum among the cell-averages of the set $\mathcal{V}_i^n$, respectively. The set $\mathcal{V}_i^n$ contains *all* the vertex neighbors of T_i^n and the element T_i^n itself. Since $\mathbf{w}_h$ is obtained as a piecewise linear reconstruction of the data, its extrema occur at the vertices of T_i^n. Hence, to compute the limiter it suffices to find for all vertices $\mathbf{x}_j$ of T_i^n

$$\Phi_{i,j} = \begin{cases} \min\left(1, \frac{\mathbf{Q}_i^{max}-\mathbf{Q}_i^n}{\mathbf{w}_{h,j}-\mathbf{Q}_i^n}\right), & \text{if } \mathbf{w}_{h,j}-\mathbf{Q}_i^n > 0 \\ \min\left(1, \frac{\mathbf{Q}_i^{min}-\mathbf{Q}_i^n}{\mathbf{w}_{h,j}-\mathbf{Q}_i^n}\right), & \text{if } \mathbf{w}_{h,j}-\mathbf{Q}_i^n < 0 \\ 1 & \text{if } \mathbf{w}_{h,j}-\mathbf{Q}_i^n = 0. \end{cases}$$

with $\mathbf{w}_{h,j} = \mathbf{w}_h(\mathbf{x}_j,t^n)$. Then, the slope limiter is defined as

$$\Phi_i = \min_j(\Phi_{i,j}).$$

Finally, second order of accuracy in *time* is achieved by an element-local predictor stage that evolves the reconstructed polynomials $\tilde{\mathbf{w}}_i(\mathbf{x},t^n)$ within each element $T_i^n(t)$ during the time interval $[t^n,t^{n+1}]$. The piecewise space-time polynomials are denoted by $\mathbf{q}_h(\mathbf{x},t)$, and are of the form

$$\mathbf{q}_h(\mathbf{x},t)|_{T_i^n} = \mathbf{Q}_i^n + \Phi_i\nabla\mathbf{Q}_i(\mathbf{x}-\mathbf{x}_i) + \partial_t\mathbf{Q}_i(t-t^n), \quad \mathbf{x}\in T_i(t),\ t\in[t^n,t^{n+1}]. \tag{4}$$

The value of $\partial_t\mathbf{Q}_i$ can be easily computed from a discrete integral form of (1) by summing over the set of edges of T_i^n, denoted by $\mathcal{E}_i$:

$$\partial_t\mathbf{Q}_i = -\sum_{e\in\mathcal{E}_i}\left(\lambda_e\mathbf{F}\left(\tilde{\mathbf{w}}_h(\mathbf{x}_e,t^n)\right)\cdot\mathbf{n}_e\right) + \mathbf{S}\left(\tilde{\mathbf{w}}_h(\mathbf{x}_i,t^n)\right). \tag{5}$$

Here, $\mathbf{x}_e$ denotes the midpoint of edge e, λ_e is the edge length and $\mathbf{n}_e$ is the outward-pointing unit normal vector; $\mathbf{x}_i$ is the barycenter of cell T_i^n.

2.2. Finite volume scheme: one step element update

Once $\mathbf{q}_h(\mathbf{x},t)$ has been computed for each T_i^n, we are in the position to introduce the one-step space-time finite volume scheme. As proposed in [9], the governing PDE (1) is first reformulated in a space–time divergence form as

$$\tilde{\nabla}\cdot\tilde{\mathbf{F}} = \mathbf{S}(\mathbf{Q}), \tag{6}$$

with

$$\tilde{\nabla} = \left(\frac{\partial}{\partial x}, \frac{\partial}{\partial y}, \frac{\partial}{\partial t} \right)^T, \qquad \tilde{\mathbf{F}} = (\mathbf{F}, \mathbf{Q}) = (\mathbf{f}, \mathbf{g}, \mathbf{Q}), \tag{7}$$

and it is then integrated in time over the space–time control volume C_i^n

$$\int_{t^n}^{t^{n+1}} \int_{T_i(t)} \tilde{\nabla} \cdot \tilde{\mathbf{F}} \, d\mathbf{x} dt = \int_{t^n}^{t^{n+1}} \int_{T_i(t)} \mathbf{S} \, d\mathbf{x} dt. \tag{8}$$

The *space–time control volume*

$$C_i^n = T_i^n(t), \quad \text{with } t \in [t^n, t^{n+1}]$$

is obtained by connecting each vertex of the element T_i^n via *straight* line segments with the corresponding vertex of T_i^{n+1}. For a graphical interpretation one can refer to Figure 1, where we have reported an example of a control volume and of the parametrization of the lateral space–time surfaces.

Now, for each control volume we have to compute its barycenter and the areas, the normal vectors, and the space–time midpoints of all its sub–surfaces.

The upper space–time sub–surface T_i^{n+1} and the lower space–time sub–surface T_i^n are the simplest, since they are orthogonal to the time coordinate. The space–time unit normal vectors read respectively $\tilde{\mathbf{n}} = (0, 0, 1)$ and $\tilde{\mathbf{n}} = (0, 0, -1)$. To compute their areas we can use the *shoelace formula* or *Gauss's area formula* which is valid for any type of polygonal element

$$|\, T_i^n \,| = \frac{1}{2} \left| \sum_{j=1}^{N\mathrm{v}(i)-1} x_j^n y_{j+1}^n + x_{N\mathrm{v}(i)}^n y_1^n - \sum_{j=1}^{N\mathrm{v}(i)-1} x_{j+1}^n y_j^n + x_1^n y_{N\mathrm{v}(i)}^n \right|. \tag{9}$$

The only thing that has to be taken into account is the periodicity of the domain: so if the domain is periodic w.r.t the y coordinate we rewrite formula (9) in the form

$$|\, T_i^n \,| = \frac{1}{2} \left| \sum_{j=1}^{N\mathrm{v}(i)} x_j^n \left(y_{j+1}^n - y_{j-1}^n \right) \right|,$$

which depends only on the signed distance between the y coordinates of the vertices. Moreover, the space–time barycenter M_i^n of each control volume C_i^n reads

$$M_i^n = \left(\frac{\mathbf{x}_i^n + \mathbf{x}_i^{n+1}}{2}, \frac{t^n + t^{n+1}}{2} \right),$$

where the spatial barycenter $\mathbf{x}_i^n = (x_i^n, y_i^n)$ of T_i^n is given by the explicit formula

$$\begin{aligned} x_i^n &= \frac{1}{6\,|T_i^n|} \sum_{j=1}^{N\mathrm{v}(i)} \left(x_j + x_{j+1} \right) \left(x_j y_{j+1} - x_{j+1} y_j \right), \\ y_i^n &= \frac{1}{6\,|T_i^n|} \sum_{j=1}^{N\mathrm{v}(i)} \left(y_j + y_{j+1} \right) \left(x_j y_{j+1} - x_{j+1} y_j \right). \end{aligned} \tag{10}$$

with the convention that $j = N\mathrm{v}(i) + 1$ coincides with $j = 1$.

Next, the $N\mathrm{v}(i)$ lateral space–time sub–surfaces of C_i^n are parametrized using a set of bilinear basis functions as

$$\partial C_{ij}^n = \tilde{\mathbf{x}}(\chi, \tau) = \sum_{k=1}^{4} \beta_k(\chi, \tau) \, \tilde{\mathbf{X}}_{ij,k}^n, \qquad 0 \le \chi \le 1, \quad 0 \le \tau \le 1, \tag{11}$$

where $\tilde{\mathbf{X}}^n_{ij,k}$ represent the physical space–time coordinates of the four vertices of ∂C^n_{ij}, and the $\beta_k(\chi,\tau)$ functions read

$$\begin{aligned}\beta_1(\chi,\tau) &= (1-\chi)(1-\tau),\\ \beta_2(\chi,\tau) &= \chi(1-\tau),\\ \beta_3(\chi,\tau) &= \chi\tau,\\ \beta_4(\chi,\tau) &= (1-\chi)\tau.\end{aligned} \tag{12}$$

The mapping in time is given by the transformation

$$t = t_n + \tau\,\Delta t, \qquad \tau = \frac{t-t^n}{\Delta t}, \tag{13}$$

hence the Jacobian matrix $J_{\partial C^n_{ij}}$ of the parametrization is

$$J_{\partial C^n_{ij}} = \begin{pmatrix} \vec{e}_x & \vec{e}_y & \vec{e}_t \\ \frac{\partial x}{\partial \chi} & \frac{\partial y}{\partial \chi} & \frac{\partial t}{\partial \chi} \\ \frac{\partial x}{\partial \tau} & \frac{\partial y}{\partial \tau} & \frac{\partial t}{\partial \tau} \end{pmatrix} = \begin{pmatrix} \tilde{\mathbf{e}} \\ \frac{\partial \tilde{\mathbf{x}}}{\partial \chi} \\ \frac{\partial \tilde{\mathbf{x}}}{\partial \tau} \end{pmatrix}. \tag{14}$$

The space–time unit normal vector $\tilde{\mathbf{n}}_{ij}$ can be evaluated computing the normalized cross product between the transformation vectors of the mapping (11), i.e.

$$|\partial C^n_{ij}| = \left|\frac{\partial \tilde{\mathbf{x}}}{\partial \chi} \times \frac{\partial \tilde{\mathbf{x}}}{\partial \tau}\right|, \quad \tilde{\mathbf{n}}_{ij} = \left(\frac{\partial \tilde{\mathbf{x}}}{\partial \chi} \times \frac{\partial \tilde{\mathbf{x}}}{\partial \tau}\right) / |\partial C^n_{ij}|, \tag{15}$$

where $|\partial C^n_{ij}|$ is the determinant of the Jacobian matrix $J_{\partial C^n_{ij}}$ and represents also the area of the lateral surfaces. Moreover, exploiting the parametrizations in (11)-(13) and choosing

$$\chi = 0.5 \;\text{ and }\; \tau = 0.5,$$

we recover the coordinates $M^n_{i,j}$ of the space–time midpoint of the lateral surfaces.

Finally, when we allow a node to slide along an edge in a *nonconforming way*, the space–time lateral surfaces have to be treated slightly differently, refer to Figure 2 for a graphic interpretation.

Consider the case of $\partial C^n_{i,j}$ with the four standard vertices and two more hanging nodes on the edges orthogonal to the time coordinate (as in the middle of Figure 2). Then the lateral surface is shared between three (not two as usual) control volumes. However it can be subdivided into two pieces, each one shared between only two control volumes, which are still trapezoidal, so each of them can be mapped into the reference element using the standard map in (11), just taking care to select in a correct way the vertices of each piece. Hence areas, normal vectors, and space–time midpoints can be computed exactly as in the conforming case but on each part, and so we will recover these data for each piece. Next, on the left and on the right of Figure 2 we have reported the two limiting cases: first, at time t^{n+1} a new node has been inserted, which at the previous time t^n did not yet exist; or vice-versa, at time t^{n+1} a hanging node is merged together with one of the other vertices and hence it disappears. In these cases the lateral surfaces can still be divided into two parts, and even if one of them is triangular it can still be treated as a degenerate quadrilateral face, so all the computations can be performed, once again, as above. The only necessary care is the availability of the coordinates of the hanging nodes also, respectively, before its creation or after its destruction (these coordinates will be settled equal respectively to those of the vertex from which the hanging node was born or those of the vertex to whom it was merged).

Note that the treatment of the nonconforming lateral space–time surfaces basically requires only to repeat the computation of the necessary geometric information over each piece and the same will hold for the flux computation, which will be simply split in several parts.

Once having computed all the relevant geometric information about each control volume C_i^n, its space–time surface

$$\partial C_i^n = \left(\bigcup_{j=1}^{N\nu(i)} \partial C_{ij}^n \right) \cup T_i^n \cup T_i^{n+1}, \tag{16}$$

and eventually of each sub–piece of ∂C_{ij}^n, we can go on with the space–time divergence form of the PDE

$$\int_{t^n}^{t^{n+1}} \int_{T_i(t)} \tilde{\nabla} \cdot \tilde{\mathbf{F}} \, d\mathbf{x}dt = \int_{t^n}^{t^{n+1}} \int_{T_i(t)} \mathbf{S} \, d\mathbf{x}dt. \tag{17}$$

The volume integral on the left-hand side of (17) can be rewritten using the Gauss theorem as

$$\int_{\partial C_i^n} \tilde{\mathbf{F}} \cdot \tilde{\mathbf{n}} \, dS = \int_{t^n}^{t^{n+1}} \int_{T_i(t)} \mathbf{S} \, d\mathbf{x}dt, \tag{18}$$

where $\tilde{\mathbf{n}} = (\tilde{n}_x, \tilde{n}_y, \tilde{n}_t)$ is the previously computed outward pointing space–time unit normal vector on the space–time surface ∂C_i^n.

The final high order ALE one–step finite volume scheme is obtained from equation (18) as

$$|T_i^{n+1}| \, \mathbf{Q}_i^{n+1} = |T_i^n| \, \mathbf{Q}_i^n - \sum_{j=1}^{N\nu(i)} \int_0^1 \int_0^1 |\partial C_{ij}^n| \tilde{\mathbf{F}}_{ij} \cdot \tilde{\mathbf{n}}_{ij} \, d\chi d\tau + \int_{t^n}^{t^{n+1}} \int_{T_i(t)} \mathbf{S}(\mathbf{q}_h) \, d\mathbf{x}dt, \tag{19}$$

where the discontinuity of the solution at the space–time sub–face ∂C_{ij}^n is resolved by an ALE numerical flux function $\tilde{\mathbf{F}}_{ij} \cdot \tilde{\mathbf{n}}_{ij}$, which computes the flux between two neighbors across the intermediate space–time lateral surface. In particular when the lateral surface is shared between more than two control volumes (as shown in Figure 2) we have to compute the fluxes across each sub-piece and sum each contribution. We use either a Rusanov–type or an Osher–type ALE flux.

Let $\mathbf{q}_h^-(\mathbf{x}, t)$ be the reconstructed numerical solution inside the element $T_i(t)$ and $\mathbf{q}_h^+(\mathbf{x}, t)$ be the reconstructed numerical solution inside one of the neighbors of T_i^n through $\partial C_{i,j}^n$; let $\mathbf{q}_h^-$ and $\mathbf{q}_h^+$ the values of these polynomials evaluated at the space-time midpoint $M_{i,j}^n$ of the considered piece of the lateral surface.

Then the expression for the Rusanov flux is given by

$$\tilde{\mathbf{F}}_{ij} \cdot \tilde{\mathbf{n}}_{ij} = \frac{1}{2} \left(\tilde{\mathbf{F}}(\mathbf{q}_h^+) + \tilde{\mathbf{F}}(\mathbf{q}_h^-) \right) \cdot \tilde{\mathbf{n}}_{ij} - \frac{1}{2} s_{\max} \left(\mathbf{q}_h^+ - \mathbf{q}_h^- \right), \tag{20}$$

where $s_{\max}$ is the maximum eigenvalue of the ALE Jacobian matrix w.r.t. the normal direction in space, i.e.

$$\mathbf{A}_{\mathbf{n}}^{\mathbf{V}}(\mathbf{Q}) = \left(\sqrt{\tilde{n}_x^2 + \tilde{n}_y^2} \right) \left[\frac{\partial \mathbf{F}}{\partial \mathbf{Q}} \cdot \mathbf{n} - (\mathbf{V} \cdot \mathbf{n}) \, \mathbf{I} \right], \qquad \mathbf{n} = \frac{(\tilde{n}_x, \tilde{n}_y)^T}{\sqrt{\tilde{n}_x^2 + \tilde{n}_y^2}}, \tag{21}$$

with $\mathbf{I}$ representing the identity matrix and $\mathbf{V} \cdot \mathbf{n}$ denoting the local normal mesh velocity.

The Osher–type flux formulation has been proposed in the Eulerian framework in [32] and has been subsequently extended to moving meshes in one and two space dimensions in [33] and [9], respectively. It reads

$$\tilde{\mathbf{F}}_{ij} \cdot \tilde{\mathbf{n}}_{ij} = \frac{1}{2} \left(\tilde{\mathbf{F}}(\mathbf{q}_h^+) + \tilde{\mathbf{F}}(\mathbf{q}_h^-) \right) \cdot \tilde{\mathbf{n}}_{ij} - \frac{1}{2} \left(\int_0^1 \left| \mathbf{A}_{\mathbf{n}}^{\mathbf{V}}(\boldsymbol{\Psi}(s)) \right| ds \right) \left(\mathbf{q}_h^+ - \mathbf{q}_h^- \right), \tag{22}$$

where we choose to connect the left and the right state across the discontinuity using a simple straight–line segment path

$$\boldsymbol{\Psi}(s) = \mathbf{q}_h^- + s \left(\mathbf{q}_h^+ - \mathbf{q}_h^- \right), \qquad 0 \le s \le 1. \tag{23}$$

The absolute value of the dissipation matrix in (22) is evaluated as usual as

$$|\mathbf{A}| = \mathbf{R}|\mathbf{\Lambda}|\mathbf{R}^{-1}, \qquad |\mathbf{\Lambda}| = \mathrm{diag}\left(|\lambda_1|, |\lambda_2|, ..., |\lambda_\nu|\right), \tag{24}$$

where $\mathbf{R}$ and $\mathbf{R}^{-1}$ denote, respectively, the right eigenvector matrix and its inverse of the ALE Jacobian $\mathbf{A}^{\mathbf{V}}_{\mathbf{n}} = \frac{\partial \mathbf{F}}{\partial \mathbf{Q}} \cdot \mathbf{n} - (\mathbf{V} \cdot \mathbf{n})\mathbf{I}$. In (19) the time step Δt is given by

$$\Delta t = \mathrm{CFL} \min_{T_i^n} \frac{d_i}{|\lambda_{\max,i}|}, \qquad \forall T_i^n \in \Omega^n, \tag{25}$$

where CFL is the Courant-Friedrichs-Levy number, d_i represents the encircle diameter of element T_i^n and $|\lambda_{\max,i}|$ is the maximum absolute value of the eigenvalues computed from the solution $\mathbf{Q}_i^n$ in T_i^n. As stated in [57], for linear stability in two space dimensions the Courant number must satisfy CFL ≤ 0.5.

We underline that the integration over a closed space–time control volume, as done above, automatically satisfies the so-called geometric conservation law (GCL), since from the Gauss theorem follows

$$\int_{\partial C_i^n} \tilde{\mathbf{n}}\, dS = 0. \tag{26}$$

The relation between (26) and the usual form of the GCL that is typically employed in the community working on Lagrangian schemes has been established in the appendix of [10]. For all the numerical test problems shown later in this paper it has been explicitly verified that property (26) holds for all elements and for all time steps up to machine precision.

2.3. Connectivity matrices

Since the core of the proposed method is the motion and the changing of the nonconforming mesh topology in time, we have to know all the connectivities of the mesh and to maintain them updated. In this way we will have enough information both to rearrange the mesh after the insertion of a new node, or the fusion of two existing nodes, and to know all the neighbors of each space–time lateral surface during the numerical flux computation.

As in the standard conforming case for each element T_i^n we save the global numbering of its vertices $V_1, \ldots, V_{N\mathrm{v}(i)}$ in row i of a matrix called `tri` in counterclockwise order, and in matrix `Elem2Edge` we store the global numbering of its edges $E_1, \ldots, E_{N\mathrm{v}(i)}$. However, in the nonconforming case, additional connectivity tables are needed, since more than two elements can share the same edge and more than two points can belong to it. For each edge E_j^n, we store the elements that share it in row j of matrix `Edge2Elem`, and all the nodes that belong to E_j^n in row j of matrix `Edge2Vertex` in such a way that the first two entries of each row contain the endpoints of the corresponding edge. Then, for each node we memorize the edge to which it belongs in `Vertex2Edge` (both if this node is an endpoint of the edge or an intermediate point) and the elements for which it is a vertex in `Vertex2Elem` (note that if a node N_i belongs to an edge of an element but it is not one of its vertices, that element will not appear in the row N_i of this last matrix). Moreover, each node has a label that indicates whether the node is free to move everywhere, if it has been doubled, or if it is constrained to slide along a particular edge, i.e. if it is a hanging node.

Besides, we allow our data structures to be completely dynamic in such a way that nodes and edges can appear and disappear in time: so rows can be added to our matrices or be nullified, and the information regarding which global numbering of nodes and edges is currently used is always available.

2.4. Shear interface detector

Since the sliding interfaces are not defined *a priori*by the user, at the beginning of each time step the algorithm has first to identify along which *edges* the shear interfaces lie, and mark the corresponding edges and nodes. Basically an edge e will be considered at the interface if the tangential velocity difference ΔV_e across e exceeds a certain threshold value κ_e. So for each edge we need to compute ΔV_e and κ_e.

Given the set of nodes S_e^n over the edge e, and the set of neighbors S_j^n of each node j, the threshold value κ_e is computed as

$$\kappa_e = \min_{j \in S_e^n} \kappa_j, \quad \text{with} \quad \kappa_j = \max_{i \in S_j^n} \left(\frac{\alpha d_i}{||J_i||} \right), \tag{27}$$

where d_i is the encircle diameter of element T_i^n, J_i is the Jacobian of the transformation that maps element T_i^n in the corresponding reference element, the considered norm is the two-norm of Frobenius divided by $\sqrt{2}$, and α is chosen in $[0, 1]$ according to the desired sensitivity of the detector. In particular if the velocity jump at the interface is very large, the value of α does not matter. Instead, where the velocity field changes smoothly, the number of interfaces, and as a consequence the number of new nodes, will be dependent on α. Moreover in the limit $\alpha \to +\infty$ we recover the standard conforming algorithm.

Once fixed the threshold value we loop over all the edges of the mesh: for each edge e we consider all its neighbors and we compute their tangential velocity with respect to e. Say, for example, that two elements $A = T_a^n$ and $B = T_b^n$ with area $|T_a^n|$ and $|T_b^n|$ share the same edge e and their tangential velocities are $v_{t,a}^n$ and $v_{t,b}^n$. If the quantity ΔV_e exceeds κ_e

$$\Delta V_e = \frac{\left| v_{t,a}^n |T_a^n| - v_{t,b}^n |T_b^n| \right|}{\left(|v_{t,a}^n| |T_a^n| + |v_{t,b}^n| |T_b^n| + 1e-14 \right)} \geq \kappa_e, \tag{28}$$

then edge e is marked as an edge at a shear interface, and the elements A and B are divided into two different groups: the elements on the left and the ones on the right with respect to this particular edge e. Afterwards, we also need to find the *nodes* that have *to be doubled* and to separate their Voronoi neighbors (the elements stored in `Vertex2Elem`) into two groups. So we loop over the nodes considering the ones which belong to an interface edge. If in their list of Voronoi neighbors there are elements from both the sides of the interface, according to the previous subdivision, we mark them and we separate their Voronoi neighbors into two groups which are stored in matrices called `Vertex2RightElem` and `Vertex2LeftElem`.

Note that the two cycles, the one over the edges and the other over the nodes, are not nested one into the other, but are run one after the other.

2.5. Node motion

At this point we are able to distinguish between nodes far away from the interfaces, hanging nodes and nodes which lie at the interface. So we loop over the nodes and according to their labels we choose what to do.

First, consider a regular non-hanging node k located in a smooth region. We compute its coordinates at the new time level t^{n+1} simply by

$$\mathbf{x}_k^{n+1} = \mathbf{x}_k^n + \Delta t \overline{\mathbf{V}}_k^n, \tag{29}$$

where $\overline{\mathbf{V}}_k^n$ is obtained using the node solver of Cheng and Shu. Cheng and Shu introduced a very simple and general formulation for obtaining the final node velocity, which is chosen to be the arithmetic average velocity among all the contributions coming from the Voronoi neighbor elements $\mathcal{V}_k^n$. Moreover, following the ideas presented in [12] we take a mass weighted average velocity among the neighborhood $\mathcal{V}_k^n$, that is,

$$\overline{\mathbf{V}}_k^n = \frac{1}{\mu_k} \sum_{T_j^n \in \mathcal{V}_k} \mu_{k,j} \overline{\mathbf{V}}_{k,j} \tag{30}$$

with

$$\mu_k = \sum_{T_j^n \in \mathcal{V}_k} \mu_{k,j}, \quad \mu_{k,j} = \rho_j^n |T_j^n|. \tag{31}$$

The local weights $\mu_{k,j}$, which are the masses of the elements T_j^n, are defined by multiplying the cell averaged value of density ρ_j^n with the cell area $|T_j^n|$. The local contributions $\overline{\mathbf{V}}_{k,j}$ in a pure Lagrangian context represent

the fluid velocity in the j^{th} neighbor of vertex k, while in the ALE framework they can be obtained either according to an arbitrary, prescribed mesh velocity function or by the local fluid velocity.

Now let us consider the nodes at the interfaces. The following considerations are carried out by supposing that each interface is separated from the others and lies on straight lines. Note, however, that the only constraint we have is a straight line interface, but we do not need to choose its position *a priori*.

2.5.1. Insertion of a new node

The first situation we encounter is a node k that has some of its Voronoi neighbors on the left of the interface (stored in `Vertex2LeftElem(k,:)`, call them *left neighbors*, $\mathcal{V}_{k,\text{left}}$) and the others on the right of the same interface (stored in `Vertex2RightElem(k,:)`, call them *right neighbors*, $\mathcal{V}_{k,\text{right}}$); these two sets of neighbors have been provided by the *interface detector* described above.

We apply the node solver of Cheng and Shu at the two sets of neighbors obtaining two different new coordinates

$$\tilde{\mathbf{x}}^{n+1}_{k,\,\text{left}} = \mathbf{x}^n_k + \Delta t \sum_{T^n_j \in \mathcal{V}_{k,\text{left}}} \frac{\mu_{k,j}}{\mu_k} \overline{\mathbf{V}}_{k,j}, \quad \text{and} \quad \tilde{\mathbf{x}}^{n+1}_{k,\,\text{right}} = \mathbf{x}^n_k + \Delta t \sum_{T^n_j \in \mathcal{V}_{k,\text{right}}} \frac{\mu_{k,j}}{\mu_k} \overline{\mathbf{V}}_{k,j}\,. \tag{32}$$

We allow this kind of nodes to move only along the interface, so basically according to their averaged tangential velocity with respect to the interface: for this reason we need to find the nearest interface edges and to project over them the coordinates in (32) obtaining thus $\mathbf{x}^{n+1}_{k,\,\text{left}}$ and $\mathbf{x}^{n+1}_{k,\,\text{right}}$.

Call the nearest interface edges belonging to the left elements e^ℓ_1 and e^ℓ_2, and the nearest interface edges belonging to the right elements e^r_1 and e^r_2 (suppose also that $e^{\ell,r}_1$ are closer to $\tilde{\mathbf{x}}^{n+1}_{k,\,\text{left}}$ than to $\tilde{\mathbf{x}}^{n+1}_{k,\,\text{right}}$).

We decide to assign $\mathbf{x}^{n+1}_{k,\text{left}}$ as new coordinate to the old node k

$$\mathbf{x}^{n+1}_k = \mathbf{x}^{n+1}_{k,\text{left}} \tag{33}$$

and to create a new node with global number k_{new} and coordinates (at time n and $n+1$)

$$\mathbf{x}^n_{k_{\text{new}}} = \mathbf{x}^n_k \quad \text{and} \quad \mathbf{x}^{n+1}_{k_{\text{new}}} = \mathbf{x}^{n+1}_{k,\,\text{right}}. \tag{34}$$

The global number k_{new} can be larger than N^n_{node} if all the numbers between 1 and N^n_{node} are currently used, otherwise we choose the first of the unused numbers (indeed if two nodes have been merged together one of their global numbers is no more used, see section 2.5.3).

Now we have to update the connectivity tables taking into account the insertion of this new node. See also Figure 3 to follow our construction.

First, in matrix `tri` we substitute k with k_{new} in all the right elements; moreover, we consider matrix `Vertex2Elem` and in row k we leave only the left elements and we put the others in row k_{new} (because now k is no more a vertex for the right neighbors).

Then we have to deal with the edges: if $e^\ell_1 = e^r_1$ we need to substitute e^r_1 with a new edge $e^r_{1_{\text{new}}}$. In matrix `Elem2Edge` all the right neighbors change e^r_1 with $e^r_{1_{\text{new}}}$, and in matrix `Edge2Elem` we insert a new row $e^r_{1_{\text{new}}}$ equal to row e^r_1 (the new edge inherits all the characteristics from the old one). The same has to be done if $e^\ell_2 = e^r_2$. The endpoints of these new edges are the endpoints of the substituted edges seen from the right (so basically there is k_{new} instead of k). The endpoints of the left edges do not change. Besides we add k as intermediate point in e^r_1 and k_{new} as intermediate point of e^ℓ_2, (note that an edge is allowed to have more than one intermediate point). In this way also matrix `Edge2Vertex` has been updated. Matrix `Vertex2Edge` is easily modified at the same time.

Finally, we have to revise the list of neighbors: in particular the edges that gained an intermediate point (e^r_1 and e^ℓ_2) gain also neighbors. In particular the new neighbors of e^r_1 are the left neighbors of e^ℓ_2 and the new neighbors of e^ℓ_2 are the right neighbors of e^r_1. This allow us to update `Edge2Elem` and `Elem2Edge`.

At the end we mark with a label the nodes which are intermediate for an edge: we call them *hanging nodes* and they are constrained to move along that edge. Note that in the case of straight slip-lines no

distinction between master and slave nodes is required, since both will move along the same straight interface. To extend the algorithm to the case of piece-wise linear interfaces, object of a future work, this distinction will be introduced in such a way that only slave nodes will be constrained to slide along edges, while the master nodes can move freely.

2.5.2. Hanging nodes

Consider a hanging node k which lies on the edge e: it is at the interface and it is a vertex only of elements lying on one side of the interface, so its Voronoi neighbors are in the same smooth region. However it is not free to move everywhere but it must slide along that edge, to avoid creation of holes or superposition of elements in the mesh.

We apply the averaged node solver of Cheng and Shu among its Voronoi neighbors, we find its new coordinates $\tilde{\mathbf{x}}_k^{n+1}$ and we project them over edge e, obtaining $\mathbf{x}_k^{n+1}$. Now, we compute also the new coordinates of the other points over edge e. If two of them are sufficiently close, we decide to merge them (see section 2.5.3), otherwise the computed coordinates $\mathbf{x}_k^{n+1}$ are the new coordinates of such a node and no update of the connectivity matrices is required.

2.5.3. Fusion of two existing nodes

Suppose we computed the new coordinates at time t^{n+1} of all the nodes k_i over the same edge e denoted by $X_{k_i}^{n+1}$, which are assumed to be already projected onto the straight line spanned by edge e. If the new coordinates of two of them, say k_1 and k_2, are too close, we decide to merge them. Moreover, if one intermediate node of edge e falls outside the edge, we decide to merge it with the closest endpoint of the edge.

Since the loop over the nodes is carried out according to the increasing global numbering of the nodes, we decide to remove the node with the largest global number (we call it *dead node*, k_{dn}) because we have not worked with it yet, and to maintain the one with the smallest global numbering (call it *fusion node*, k_{fn}) assigning to it as new coordinates the average between $\mathbf{x}_{k_1}^{n+1}$ and $\mathbf{x}_{k_2}^{n+1}$

$$\mathbf{x}_{k_{\text{fn}}}^{n+1} = \frac{\mathbf{x}_{k_1}^{n+1} + \mathbf{x}_{k_2}^{n+1}}{2}. \tag{35}$$

We assign the same coordinates also to the dead node

$$\mathbf{x}_{k_{\text{dn}}}^{n+1} = \frac{\mathbf{x}_{k_1}^{n+1} + \mathbf{x}_{k_2}^{n+1}}{2}. \tag{36}$$

Now, we need to update the connectivity tables. See also Figure 4 to follow our construction.

This process is somehow more complicated than the nodes splitting. Indeed when we insert a new node at time t^{n+1} we only add information without losing anything about the previous time step, and even if it is true that the right neighbors of a doubled node k change their node k with a new one k_{new}, we can dispose of all its reference simply by giving to k_{new} at time t^n the same coordinates of k, see also (32). On the contrary, when we remove a node we lose all the reference to it, reference that, only for time t^{n+1}, we still need during the computation of the interface fluxes in the finite volume scheme (it is for this reason that in (36) we have assigned the coordinates $\mathbf{x}_{k_{\text{dn}}}^{n+1}$ even to the dead node). So we decide to duplicate some of the connectivity tables, creating `triNew`, `Elem2EdgeNew`, `Edge2ElemNew`, `Edge2VertexNew`, and `Vertex2ElemNew`. During the insertion procedure we modify in the same way both the old and the new matrices, while during the fusion we modify only the `new` matrices. Hence we can use the old ones in the finite volume scheme, because they store all the needed information (for example they refer both to the dead and the fusion node which have the same coordinates at the new time t^{n+1}), while when we advance in time, to t^{n+2}, we maintain updated only the new ones because the information about two previous time steps are no longer necessary and so we can overwrite the old connectivity matrices with the new ones.

First, in matrix `triNew` we substitute k_{dn} with k_{fn} in all the neighbors of the dead node; moreover, we consider matrix `Vertex2ElemNew`, in row k_{fn} we put both the neighbors of the dead and the fusion node and we nullify row k_{dn}. We do the same with matrix `Vertex2EdgeNew`: we nullify row k_{dn} and we put in row k_{fn} all the edges that contain k_{fn} or k_{dn}.

Then all the edges that contain k_{dn} substitute it with k_{fn} (in matrix `Edge2VertexNew`), whereas the edges with both k_{dn} and k_{fn} (that we memorize in a list `Edge[dn-fn]`) remove k_{dn}. We note that merging k_{dn} and k_{fn} we are removing the segment in between, so we look for the edges that contain it (listed in `Edge[dn-fn]`) and its neighbor elements that we list in `Elem[dn-fn]`. We update now matrix `Edge2ElemNew` because the edges in `Edge[dn-fn]` have no more one of the neighbors in `Elem[dn-fn]` .

Afterward we check if the absence of this segment makes some edges in `Edge[dn-fn]` equal: in this case we remove one of them (the one with the largest global number) and we update correspondingly the new connectivity matrices.

Besides we modify the labels telling us if a node is hung to some edges and which nodes and edges are currently existing. This last passage prevents us to work again with disappeared nodes and allows us to reuse their global numbering when we want to insert a new node or a new edge.

3. Numerical results

In this section, we solve a large set of numerical tests in order to validate the presented nonconforming direct ALE scheme. The robustness of the method is checked both on smooth and discontinuous problems related to the shallow water equations written in Cartesian and in polar coordinates. The test cases are carried out using either the Rusanov or the Osher type flux, the value of α in (27) is always taken equal to $\alpha = 1$ unless otherwise specified, and the CFL number is chosen as CFL= 0.3. Furthermore, the order of convergence is verified first fixing for the mesh motion an arbitrary velocity, then in the case of a steady vortex in equilibrium using the local fluid velocity.

3.1. Sanity checks: pure sliding

The numerical examples reported in this section are sanity checks testing the robustness of the method and its ability to maintain straight slip-line interfaces. We consider the shallow water equations, which can be cast into form (1) with

$$\mathbf{Q} = \begin{pmatrix} h \\ hu \\ hv \end{pmatrix}, \quad \mathbf{f} = \begin{pmatrix} hu \\ hu^2 + \frac{1}{2}gh^2 \\ huv \end{pmatrix}, \quad \mathbf{g} = \begin{pmatrix} hv \\ huv \\ hv^2 + \frac{1}{2}gh^2 \end{pmatrix}, \tag{37}$$

over a computational domain $\Omega(t_0) = [-2, 2] \times [0, 4]$.

First, we take as initial condition

$$\mathbf{Q}(\mathbf{x}, 0) = \begin{cases} (1, 0, -2) & \text{if} \quad x \leq 0, \\ (1, 0, 2) & \text{if} \quad x > 0, \end{cases} \tag{38}$$

which also coincides with the exact solution at any time.

We impose *wall* boundary conditions on the left and on the right side of the domain, respectively, whereas at the top and at the bottom of the domain we impose *transmissive* boundary conditions. In Figure 5 we show the numerical results over a triangular mesh and then over a mixed mesh composed of both, triangular and quadrilateral elements. The chosen mesh velocity coincides exactly with the fluid velocity, as in a pure Lagrangian context. At each time step we have verified that the total water volume is conserved up to machine precision both locally and globally and that relation (26), the GCL, is verified also up to machine precision.

Then we consider as initial condition

$$\mathbf{Q}(\mathbf{x}, 0) = (1, 0, 0.5 \,\text{floor}\,(2x)) \quad -2 \leq x \leq 2, \tag{39}$$

and we run our algorithm until a final time $t = 0.7$ with different *threshold* values, see (27), in such a way that there will be a different number of interfaces along which nodes have to be doubled and merged in time. The discretization of the computational domain is reported in Figure 6. Also in this case we reach the exact solution (that is the initial condition translated in the motion direction), the total volume of water is conserved and relation (26) is verified up to machine precision at each time step and on each element.

Finally, we want to show that the interface can be along any straight line (provided that edges lie over this line): we take as initial condition

$$\mathbf{Q}(\mathbf{x}, 0) = \begin{cases} (1, -1, 1) & \text{if} \quad x + y - 2 \leq 0, \\ (1, 1, -1) & \text{if} \quad x + y - 2 > 0, \end{cases} \tag{40}$$

and in Figure 7 we report the computational domain discretization at different times. Again, the numerical solution matches the exact one and as expected, the total volume is conserved and equation (26) is satisfied up to machine precision.

3.2. Periodic boundary conditions

The tests reported in the previous section can be run also by imposing periodic boundary conditions on the top and at the bottom of the computational domain. In Figure 8 we show the discretization of the computational domain at time $t = 100.2$ for the initial conditions in (38) and in (39). We would like to underline that no distortion of the mesh elements appears even after a very long computational time, and as a direct consequence the time steps remains almost constant during the computation. As always in this type of test cases the volume conservation holds and the numerical solution is equal to the exact one up to machine precision.

3.3. Riemann problem

Let us now consider as initial condition a Riemann problem with a discontinuity in the water level

$$\mathbf{Q}(\mathbf{x}, 0) = \begin{cases} (1, 0, 0) & \text{if} \quad x \leq 0, \\ (0.5, 0, 0) & \text{if} \quad x > 0, \end{cases} \tag{41}$$

that originates a left-traveling rarefaction fan and a right-moving shock wave. We decided to move the mesh with an arbitrary velocity function

$$\mathbf{v} = (\, 0, \; 0.5 \,\text{floor}\,(2x)\,) \quad -2 \leq x \leq 2,$$

in order to check the robustness of the algorithm also in the presence of discontinuities. We imposed periodic boundary conditions on the top and on the bottom of the square, and wall boundary conditions on the left and on the right. The final discretization of the computational domain together with the comparison between the numerical and the exact solution are depicted in Figure 9 both for the first order accurate scheme (i.e. without the MUSCL-Hancock strategy for the reconstruction) and the second order accurate scheme.

3.4. Convergence test

To verify the order of convergence of the proposed method we study the passive transport of a quantity c, that at time $t = 0$ is taken equal to a Gaussian profile and then will be passively transported in the direction

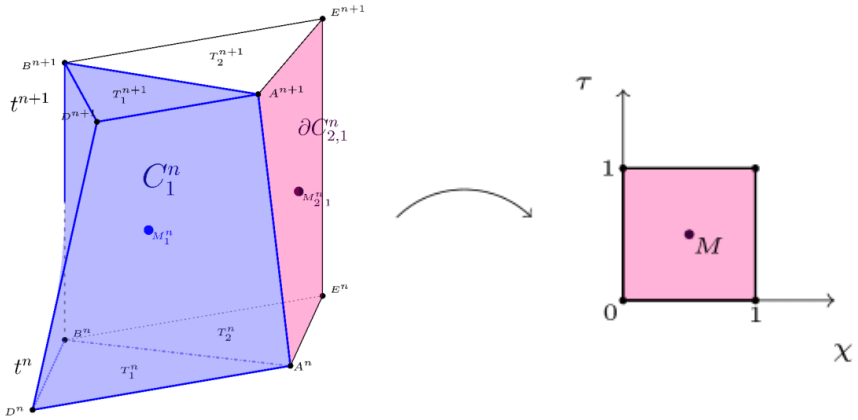

Figure 1: Left. In blue we show the physical space–time control volume C_1^n obtained by connecting via straight line segments each vertex of T_1^n with the corresponding vertex of T_1^{n+1}, and its space-time midpoint M_1^n. In pink we show one of the lateral surfaces of C_2^n, $\partial C_{2,1}^n$, together with its space–time midpoint $M_{2,1}^n$. Right. The reference system (χ, τ) adopted for the bilinear parametrization of the lateral surfaces ∂C_{ij}^n.

$O1$				$O2$			
mesh points	$h(\Omega(t_f))$	ϵ_{L_2}	$O(L_2)$	mesh points	$h(\Omega(t_f))$	ϵ_{L_2}	$O(L_2)$
12×12	1.95E-01	1.44E-01	-	12×12	1.95E-01	4.96E-02	-
24×24	9.78E-02	7.58E-02	0.93	24×24	9.78E-02	1.23E-02	2.02
40×40	5.88E-02	4.69E-02	0.94	40×40	5.88E-02	4.24E-03	2.10
80×80	2.95E-02	2.41E-02	0.97	80×80	2.95E-02	1.01E-03	2.09
120×120	1.98E-02	1.62E-02	0.99	120×120	1.98E-02	4.51E-04	2.01

Table 1: Numerical convergence results for the passive transport of a Gaussian profile. The error norms refer to the variable c at time $t = 0.5$. On the left we report the result for the first order method (i.e. without using the MUSCL-Hancock reconstruction procedure) and on the right using the second order accurate scheme.

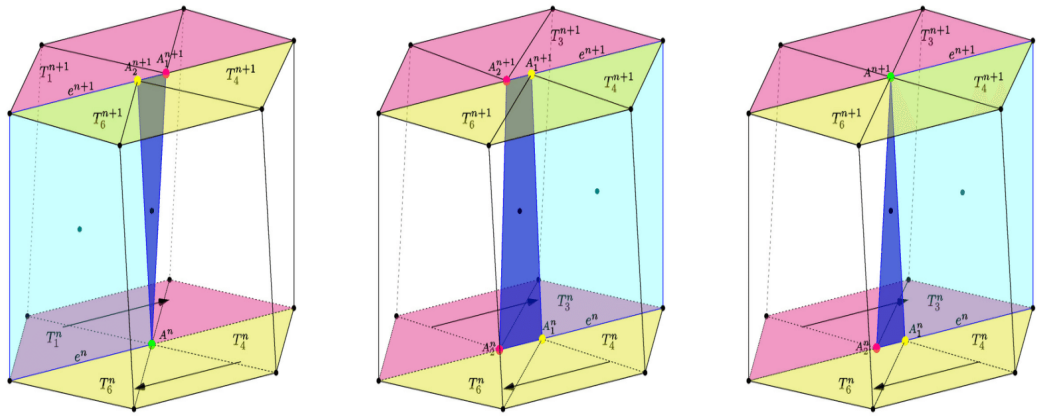

(a) Insertion of a new node (b) Motion of hanging nodes (c) Fusion of two existing nodes

Figure 2: Suppose that at time t^n across the pink and the yellow elements the tangential fluid velocity changes sharply, as suggested by the arrows; at t^{n+1} the pink elements will move in one direction and the yellow ones will move in the opposite direction. In (a) at time t^n we have a conforming mesh, but in order to avoid a severe mesh distortion in the following time steps we decide to double the green node A^n. So at time t^{n+1} there are both A_1^{n+1} and A_2^{n+1}: A_1^{n+1} is a vertex for the pink elements and A_2^{n+1} is a vertex for the yellow elements. Moreover A_2^{n+1} is hung to edge e^{n+1}. So the blue lateral face of T_i^n, which has e^n and e^{n+1} as bases, is composed by two pieces: the one in light blue which is trapezoidal and touches elements T_1 and T_6, and the one in dark blue which is triangular and touches elements T_1 and T_4. Note in particular that we need to compute the flux between T_1 and T_4 during the interval $[t^n, t^{n+1}]$ even if at time t^n they were not in contact. In (b) we show the intermediate situation where a hanging node slides along an edge. In this case the blue surface is still divided into two parts and it is shared between three elements T_3, T_4 and T_6, so the computation of two fluxes will be required. In order to compute the fluxes and to maintain the second order of accuracy of the entire method the reconstruction polynomial $\mathbf{q}_h(\mathbf{x}, t)$ will be evaluated at the midpoints of each of the part of the lateral surface. Finally, in (c) we report the last limiting case: A_1^n and A_2^n are close and at t^{n+1} will be even closer since they are moving one towards the other, so we decide to merge them and to restore the conforming and simpler situation, in particular to avoid that A_1^n will leave edge e^{n+1} at time t^{n+1}. Eventually A^{n+1} could be doubled again at t^{n+2} if the tangential velocity difference across the interface is sufficiently large.

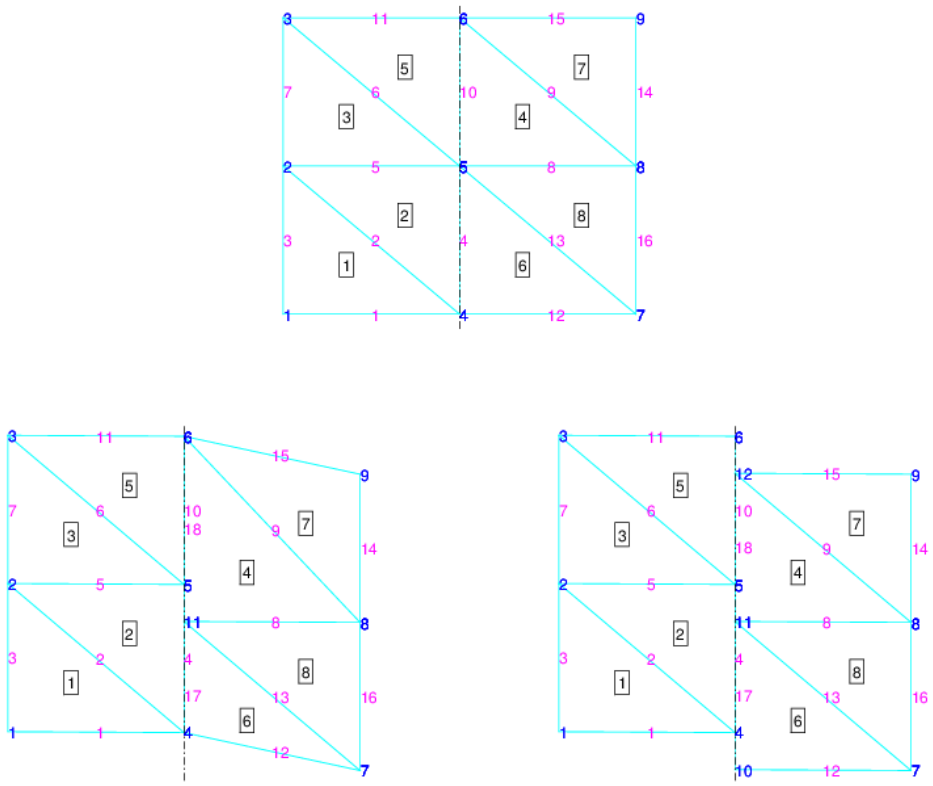

Figure 3: Example of how to double a node. At the top we show the situation before a nonconforming motion, and at the bottom after the motion and the corresponding update of the connectivity matrices. Precisely at the bottom on the left we have supposed to move in a nonconforming way only one of the nodes at the interface (for this reason the mesh is deformed, but we did it only to explain clearly one step of the algorithm), while the realistic motion of all the nodes at the interface is shown on the right. The black vertical dotted line represents the interface: suppose that the elements on the left $\{1, 2, 3, 5\}$ move with velocity $\mathbf{v} = (0, 2)$ and the elements on the right $\{4, 6, 7, 8\}$ move with velocity $\mathbf{v} = (0, -2)$. We want to double vertex number $k = 5$, so we insert a new node $k_{\text{new}} = 11$. The nearest interface edges on which we project the new coordinates of node 5 are $e_1^\ell = e_1^r = 10$ and $e_2^\ell = e_2^r = 4$. Note that edges $e_1^{\ell,r}$ are closer to k than to k_{new}. Since the edges from the left and from the right are equal we create two new edges $e^r_{1_{\text{new}}} = 18$ and $e^r_{2_{\text{new}}} = 17$. The endpoints of edges 10 and 4 remain untouched. Edge 4 gains an intermediate point, the node 11, and edge 18 gains the node 5. To better understand we list now the vertices of each edge at the end of the updating process (first we write the endpoints and then, if existing, the intermediate points): $e_1^\ell = 10 \to \{5, 8\}$, $e_2^\ell = 4 \to \{4, 5, 11\}$, $e_1^r = 18 \to \{11, 6, 5\}$ and $e_2^r = 17 \to \{4, 11\}$. Finally, elements $\{1, 3, 5, 6, 7, 8\}$ maintain the same edge neighbors, while the neighbors of elements 2 and 4 are augmented: indeed edge 4 has neighbors $\{2, 6, 4\}$ and edge 18 has neighbors $\{4, 5, 2\}$. Note that the situation on the right appears to be more complicated only because also nodes 4 and 6 have been doubled and so the corresponding update of the connectivity matrices has been done.

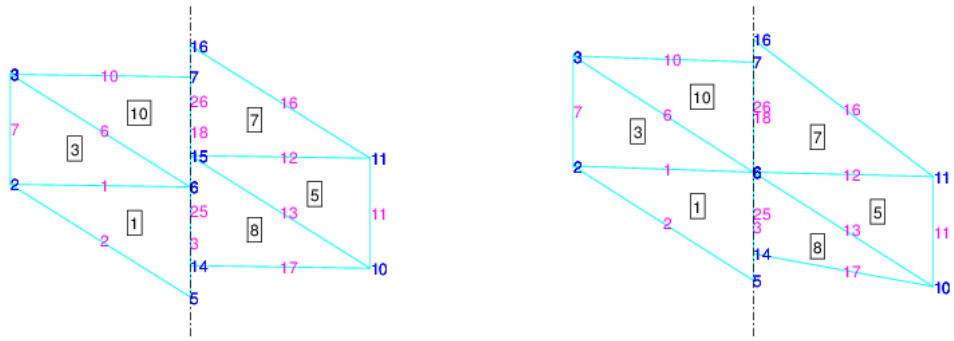

Figure 4: Example of how to merge two existing nodes. The black dotted line represents the interface: suppose that the elements on the left $\{1, 3, 10\}$ move with positive velocity and the elements on the right $\{5, 7, 8\}$ move with negative velocity. On the left we show the situation at time t^n and on the right at time t^{n+1}. Nodes 6 and 15 at t^{n+1} will be so close that we decide to merge them (as in the previous example, for the sake of clarity, we present on the right the situation after the fusion of only two nodes). We maintain the smallest global number so $k_{\text{fn}} = 6$ and we remove $k_{\text{dn}} = 15$. In `triNew` elements $\{5, 7, 8\}$ substitute $k_{\text{dn}} = 15$ with $k_{\text{fn}} = 6$. Note that in `tri` nothing changes, so some elements refer to node 6 and some other to node 15, but everything works because at time t^{n+1} they have the same new coordinates $X^{n+1}_{k_{\text{dn}}} = X^{n+1}_{k_{\text{fn}}}$ and at the successive time step t^{n+2} `tri` will no longer exist because it will be overwritten by `triNew`. In row k_{fn} of matrix `Vertex2ElemNew` there are listed elements $\{1, 3, 5, 7, 8, 10\}$, while row k_{dn} is empty. In row k_{fn} of matrix `Vertex2EdgeNew` there are edges $\{1, 3, 6, 12, 13, 18, 25, 26\}$, while row k_{dn} is empty. List `Edge[dn-fn]` contains edges $\{18, 25\}$ and list `Elem[dn-fn]` contains elements $\{8, 10\}$. Knowing these lists we can update matrices `Edge2ElemNew` because we remove element 8 from the neighbor of edge 18 and element 10 from the neighbors of edge 25. In this case even if we removed the segment $\overline{6, 15}$ no edge becomes equal so we do not need to merge edges neither to update `Elem2EdgeNew`.

of the fluid flow without changing its shape. The PDE system describing this situation is obtained from the standard shallow water equations (37) with the addition of the concentration c of a passive tracer,

$$\mathbf{Q} = \begin{pmatrix} h \\ hu \\ hv \\ hc \end{pmatrix}, \quad \mathbf{f} = \begin{pmatrix} hu \\ hu^2 + \frac{1}{2}gh^2 \\ huv \\ huc \end{pmatrix}, \quad \mathbf{g} = \begin{pmatrix} hv \\ huv \\ hv^2 + \frac{1}{2}gh^2 \\ hvc \end{pmatrix}. \tag{42}$$

We fix the following initial condition

$$\mathbf{Q}(\mathbf{x}, 0) = \left(1, u, 0, 1 + \mathrm{e}^{\frac{-0.5\left(x^2 + (y - 0.5\,p)^2\right)}{0.5^2}}\right), \quad -2 \le x \le 2, \quad 0 \le y \le p, \tag{43}$$

where we use a fluid velocity of $u = 1$ and where we have taken the period $p = 4$. The mesh is moved with the velocity

$$\mathbf{V} = (0,\ 0.5\,\mathrm{floor}\,(x)) \quad -2 \le x \le 2, \tag{44}$$

according to the ALE framework, where the mesh velocity can be chosen arbitrarily. We prescribed periodic boundary conditions on the upper and lower side of the rectangular domain, and wall boundary conditions on the left and right sides.

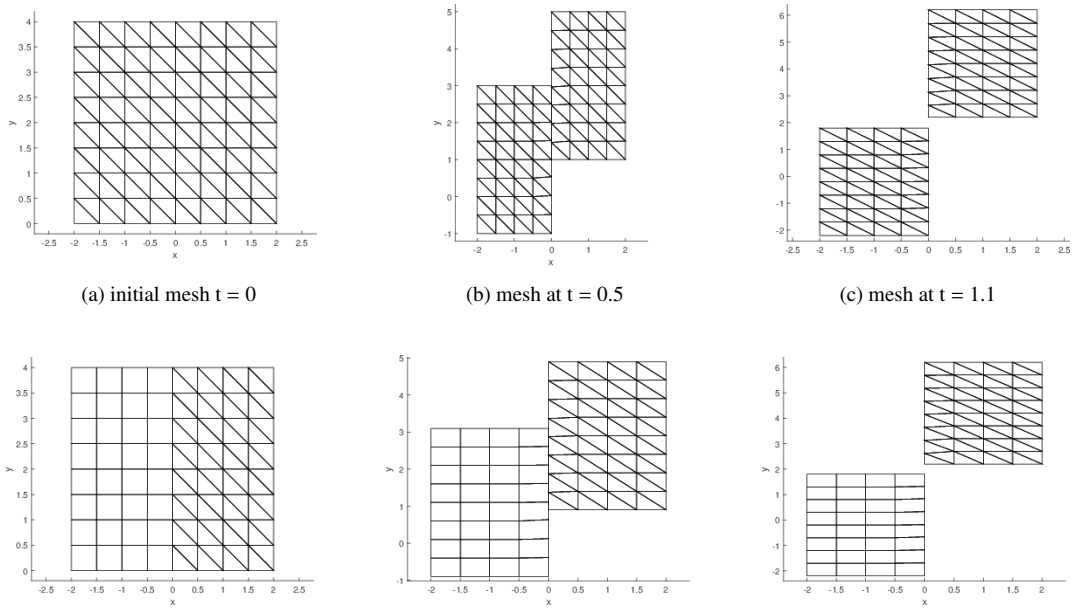

(a) initial mesh t = 0 (b) mesh at t = 0.5 (c) mesh at t = 1.1

(d) initial mesh t = 0 (e) mesh at t = 0.4 (f) mesh at t = 1.1

Figure 5: Slide lines test case with initial condition as in Equation (38). The mesh is moved with the local fluid velocity, which at $x = 0$ is discontinuous: so nodes over there are handled in a nonconforming way. At the top we show the results obtained employing a triangular mesh and at the bottom using a mesh made of both triangular and quadrilateral elements. We report the mesh at three different computational times: note that the computational domain can also be split in two non connected parts. The level of the water, the total area and the total volume are conserved at any time step, and the solution coincides with the exact one up to machine precision.

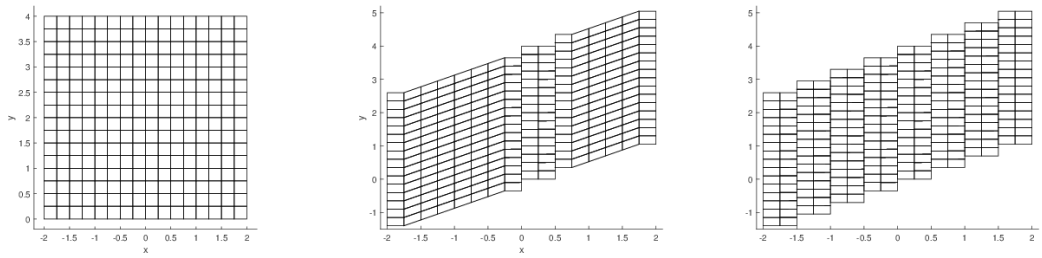

(a) initial mesh t = 0 (b) final mesh with $\alpha = 1$ (c) final mesh with $\alpha = 0.4$

Figure 6: Slide lines test case with initial condition as in Equation (39). We start with a conforming quadrilateral mesh; using a value of $\alpha = 1$ in (27) we obtain only two slip-lines (at $x = 0$ and $x = 0.5$), whereas using $\alpha = 0.4$, which makes the detector more strict, the mesh slides along each straight line where the fluid velocity changes.

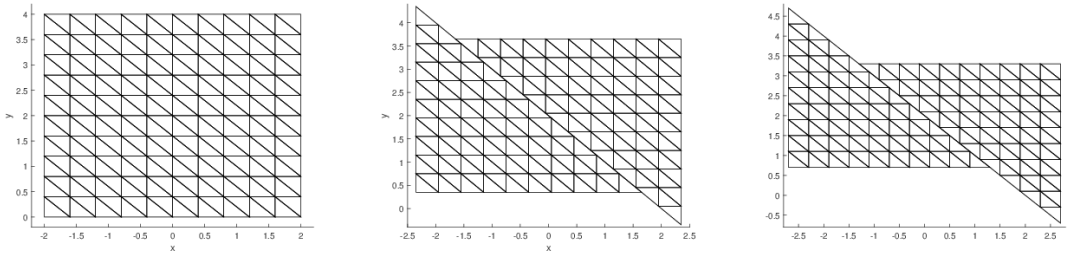

(a) initial mesh t = 0 (b) mesh at t = 0.35 (c) mesh at t = 0.7

Figure 7: Oblique slide line. We show the discretization of the computational domain at three different times. The corresponding numerical solution matches the exact one.

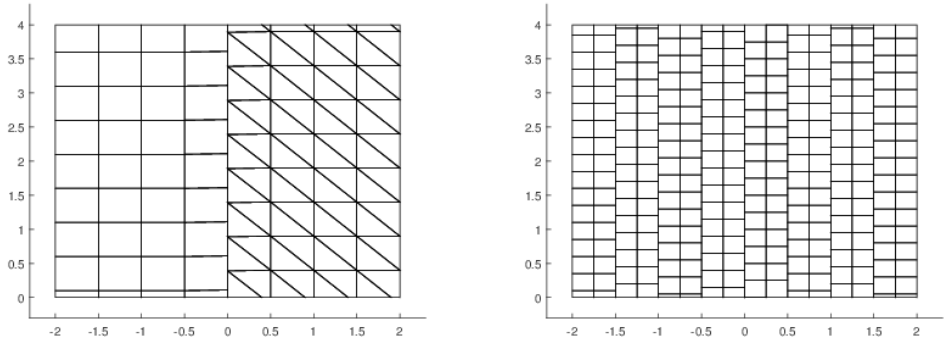

Figure 8: Slide lines with periodic boundary conditions. We report the final computational domain at time $t = 100.2$ corresponding to the initial condition in (38) on the left, and the one corresponding to the initial condition in (39) on the right. No distortion of the computational domain appears neither at the interfaces, and the numerical solution coincides with the exact one.

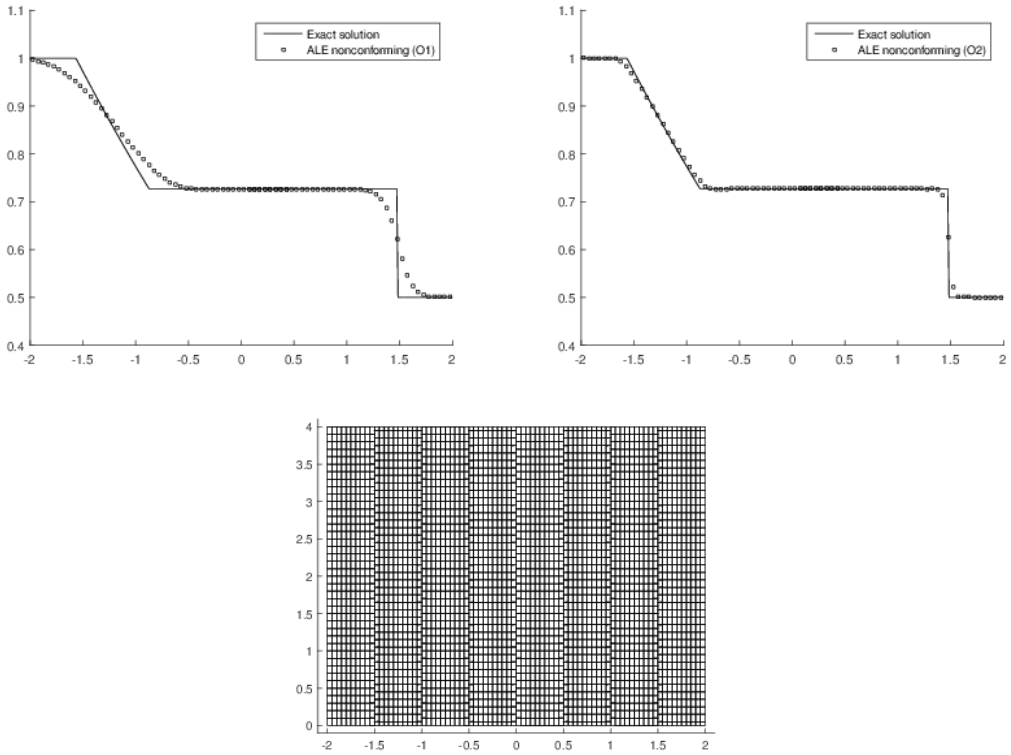

Figure 9: Riemann problem with an arbitrary mesh velocity. Taking $\alpha = 0.4$ in (27) the algorithm identifies 7 interfaces which are then handled in a non conforming way. In the figure we report the final discretization of the computational domain, and the comparison between the exact solution and the numerical solutions obtained with our nonconforming method both employing and not employing the MUSCL-Hancock strategy.

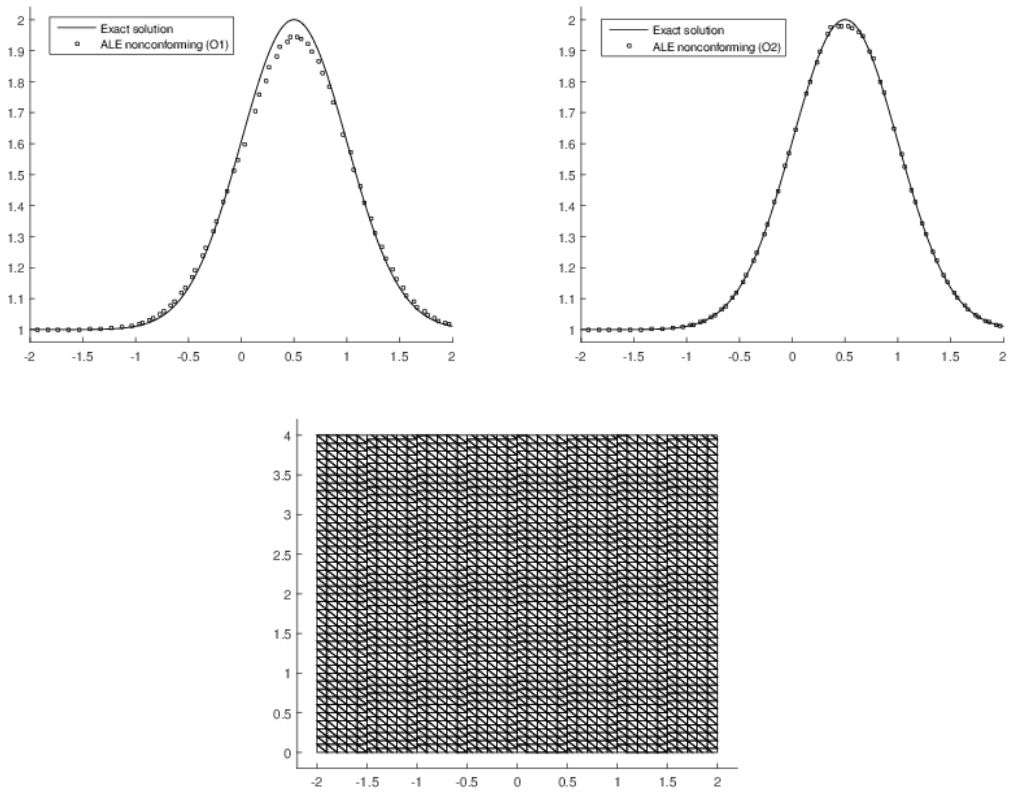

Figure 10: At the top we compared the exact solution for the transported quantity c with the one computed with the basic first order algorithm (left) and the one obtained employing also the MUSCL-Hancock strategy (right), which is second order accurate. The comparison is done at time $t = 0.5$ taking a cut of the profile of c corresponding to $y = 2$. At the bottom we show the discretization of the computational domain at time $t = 0.5$.

Since the exact solution is known ($\mathbf{Q}(\mathbf{x},t) = \mathbf{Q}(\mathbf{x} - ut, 0)$) and it is smooth, we can verify the order of convergence of our method. In Table 1 we report the order of convergence of the basic first order finite volume method, and of its second order extension that uses the MUSCL-Hancock strategy for the reconstruction procedure in space and time. Moreover, in Figure 10 we compare the numerical solution for the variable c with the profile of the exact solution and we show the mesh at the final time.

3.5. Steady vortex in equilibrium

To show that our method is also robust enough for vortex flows, we simulate the case of a steady vortex in equilibrium and we will compare the results obtained with our nonconforming method with a standard conforming algorithm (without any rezoning technique) looking at the differences after long simulation times.

First, we need to rewrite the shallow water equation in (37) in polar coordinates. Consider the usual relation between polar (ρ, φ) and Cartesian (x, y) coordinates

$$\begin{cases} x = \rho\cos\varphi \\ y = \rho\sin\varphi\,, \end{cases} \tag{45}$$

and the corresponding relation for the derivatives

$$\begin{cases} \frac{\partial}{\partial x} &= \cos\varphi\,\frac{\partial}{\partial\rho} - \frac{\sin\varphi}{\rho}\,\frac{\partial}{\partial\varphi} \\ \frac{\partial}{\partial y} &= \sin\varphi\,\frac{\partial}{\partial\rho} + \frac{\cos\varphi}{\rho}\,\frac{\partial}{\partial\varphi} \end{cases} \tag{46}$$

and let u_ρ and u_φ be respectively the radial and the tangential component of the velocity, linked to u and v by

$$\begin{cases} u = \cos\varphi\,u_\rho - \sin\varphi\,u_\varphi, \\ v = \sin\varphi\,u_\rho + \cos\varphi\,u_\varphi\,. \end{cases} \tag{47}$$

Now by substituting into (37) the expressions given in (47) and (46), after some calculations, we derive a new set of hyperbolic equations

$$\begin{cases} \frac{\partial\rho h}{\partial t} + \frac{\partial\rho h u_\rho}{\partial\rho} + \frac{\partial h u_\varphi}{\partial\varphi} = 0, \\ \frac{\partial\rho h u_\rho}{\partial t} + \frac{\partial}{\partial\rho}\left(\rho h u_\rho^2 + \frac{1}{2}g\rho h^2\right) + \frac{\partial h u_\rho u_\varphi}{\partial\varphi} = h u_\varphi^2 + \frac{1}{2}g h^2, \\ \frac{\partial\rho h u_\varphi}{\partial t} + \frac{\partial\rho h u_\rho u_\varphi}{\partial\rho} + \frac{\partial}{\partial\varphi}\left(h u_\varphi^2 + \frac{1}{2}g h^2\right) = -h u_\rho u_\varphi, \end{cases} \tag{48}$$

which, however, does not yet fit into the general form (1), since the fluxes in the above system depend explicitly on the spatial coordinate ρ (i.e. the system is not autonomous). Thus, we add the following trivial equation to the system

$$\frac{\partial\rho}{\partial t} = 0, \tag{49}$$

obtaining

$$\begin{cases} \frac{\partial\rho h}{\partial t} + \frac{\partial\rho h u_\rho}{\partial\rho} + \frac{\partial h u_\varphi}{\partial\varphi} = 0, \\ \frac{\partial\rho h u_\rho}{\partial t} + \frac{\partial}{\partial\rho}\left(\rho h u_\rho^2 + \frac{1}{2}g\rho h^2\right) + \frac{\partial h u_\rho u_\varphi}{\partial\varphi} = h u_\varphi^2 + \frac{1}{2}g h^2, \\ \frac{\partial\rho h u_\varphi}{\partial t} + \frac{\partial\rho h u_\rho u_\varphi}{\partial\rho} + \frac{\partial}{\partial\varphi}\left(h u_\varphi^2 + \frac{1}{2}g h^2\right) = -h u_\rho u_\varphi, \\ \frac{\partial\rho}{\partial t} = 0. \end{cases} \tag{50}$$

The vector of the conserved variables, the non linear flux, and the source can now be written as

$$\mathbf{Q} = \begin{pmatrix} \rho h \\ \rho h u_\rho \\ \rho h u_\varphi \\ \rho \end{pmatrix}, \quad \mathbf{f} = \begin{pmatrix} \rho h u_\rho \\ \rho h u_\rho^2 + \frac{1}{2}g\rho h^2 \\ \rho h u_\rho u_\varphi \\ 0 \end{pmatrix}, \quad \mathbf{g} = \begin{pmatrix} h u_\varphi \\ h u_\rho u_\varphi \\ h u_\varphi^2 + \frac{1}{2}g h^2 \\ 0 \end{pmatrix}, \quad S = \begin{pmatrix} 0 \\ h u_\varphi^2 + \frac{1}{2}g h^2 \\ -h u_\rho u_\varphi \\ 0 \end{pmatrix}. \tag{51}$$

and the Jacobian matrices, necessary for the computation of the ALE Jacobian matrix in (21), are

$$A_1 = \frac{\partial \mathbf{f}}{\partial \mathbf{Q}} = \begin{pmatrix} 0 & 1 & 0 & 0 \\ -u_\rho^2 + gh & 2u_\rho & 0 & -\frac{1}{2}gh^2 \\ -u_\rho u_\varphi & u_\varphi & u_\rho & 0 \\ 0 & 0 & 0 & 0 \end{pmatrix}, \quad A_2 = \frac{\partial \mathbf{g}}{\partial \mathbf{Q}} = \begin{pmatrix} 0 & 0 & \frac{1}{\rho} & -\frac{hu_\varphi}{\rho} \\ -\frac{u_\rho u_\varphi}{\rho} & \frac{u_\varphi}{\rho} & \frac{u_\rho}{\rho} & -\frac{hu_\rho u_\varphi}{\rho} \\ -\frac{u_\varphi^2}{\rho} + g\frac{h}{\rho} & 0 & \frac{2u_\varphi}{\rho} & -\frac{hu_\varphi^2}{\rho} - g\frac{h^2}{\rho} \\ 0 & 0 & 0 & 0 \end{pmatrix}. \tag{52}$$

We choose the following initial condition

$$\mathbf{Q}(\rho, \varphi, 0) = \begin{cases} h = 1 - \frac{1}{2g}\mathrm{e}^{-(\rho^2-1)}, \\ u_\rho = 0, \\ u_\varphi = \rho \mathrm{e}^{0.5(\rho^2-1)}, \end{cases} \tag{53}$$

which is a stationary solution of (50), and so coincides with the exact solution at any time. We performed our test both with the Osher and the Rusanov fluxes and with a mesh made of triangles, quadrilaterals or both.

The considered computational domain is $\Omega(\rho, \varphi) = [0.2, 2] \times [0, 2\pi]$ which is easily mapped to the annulus with radius $[0.2, 2]$. Indeed the choice of considering the shallow water equations in polar coordinates allows us to study the vortex over a rectangular domain with periodic boundary conditions (at $\varphi = 0$ and $\varphi = 2\pi$) instead of dealing with circles. At $\rho = 0.2$ and $\rho = 2$ we have imposed reflexive boundary conditions. In particular using the polar coordinates the detected shear interfaces lie over straight lines and so they are perfectly handled by our algorithm. The images presented in this section are then obtained by mapping back our results to Cartesian coordinates, as shown in Figure 11.

First, Table 2 confirms the designed order of convergence of our algorithm in multiple situations: so primarily we can say that the mesh motion does not affect the standard order of convergence of the MUSCL-Hancock strategy and moreover this shows once again that the numerical flux computation, even at the nonconforming interfaces, is carried out correctly. The numerical solution at $t = 15$ is compared with the analytical one in Figure 12.

Then we would like to compare the results with a standard conforming method. First, let us underline that when the velocity changes even within the same element the only way to overcome the mesh distortion would be to split the element itself. For this reason, where the velocity field changes smoothly and as a consequence the shear flow affects all the vertices of the same element, at a certain time the mesh will become invalid even in the nonconforming case. This would not happen if the velocity field were uniform within each element, i.e. if each element moved all its vertices with the same velocity, e.g. the velocity of the barycenter.

The main difference between the new nonconforming algorithm and a conventional conforming method is the final time at which the computation stops due to an invalid mesh, and the time step restriction that depends on the smallest encircle diameter of the elements.

In Table 3 we report the employed number of time steps and their dimension for different kinds of meshes and at different times. We remark that a larger value of Δt decreases the required number of time steps and in this way also the total amount of computational time. The last results of each group refer to the moment at which the algorithm breaks due to an invalid mesh: one can easily see that the nonconforming method is able to run almost eight times longer than a conventional ALE method on conforming grids.

Finally, looking at Figure 13 one can appreciate that the conforming method destroys the mesh immediately and then breaks, whereas the new nonconforming algorithm maintains a high quality mesh for a very long time, even with a very coarse mesh.

4. Conclusion

Up to now we have developed a robust second order direct ALE finite volume scheme on moving unstructured nonconforming meshes under the constraint of straight slip-line interfaces. The presented

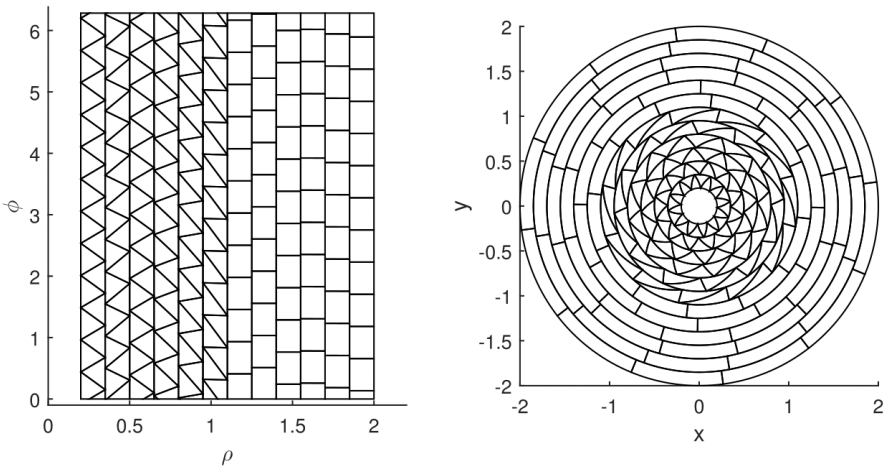

Figure 11: Domain discretization at time $t = 15$. On the left we report the grid in polar coordinates where the shear discontinuities lie over straight lines. On the right the corresponding grid in Cartesian coordinates.

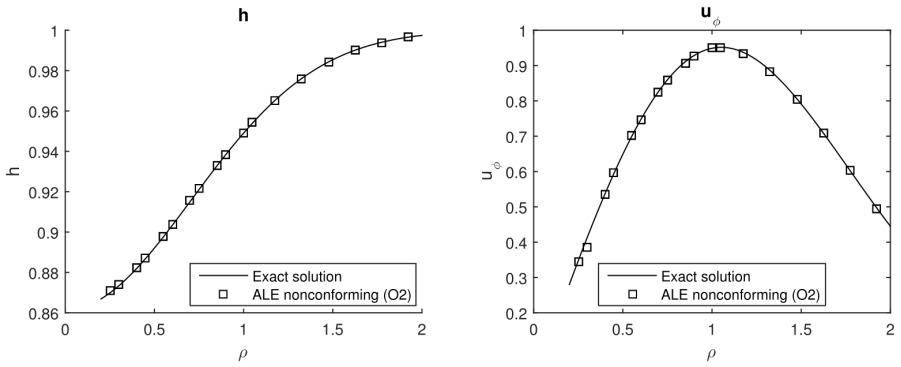

Figure 12: Comparison between analytical solution and second-order accurate numerical results for the water level h (left) and the tangential component of the velocity u_φ (right), with $\varphi = 2\pi$ and $\rho \in [0.2, 2]$.

$O2$, Osher flux, quadrilateral elements				$O2$, Rusanov flux, triangular elements			
mesh points	$h(\Omega(t_f))$	ϵ_{L_2}	$O(L_2)$	mesh points	$h(\Omega(t_f))$	ϵ_{L_2}	$O(L_2)$
12×12	2.33E-01	1.36E-03	-	20×20	7.18E-02	5.97E-04	-
24×24	1.17E-01	3.42E-04	1.99	30×30	5.21E-02	2.54E-04	2.11
32×32	8.74E-02	1.94E-04	1.97	40×40	3.91E-02	1.43E-04	2.01
44×44	6.36E-02	1.03E-04	1.98	55×55	2.84E-02	7.76E-05	1.91
60×60	4.66E-02	5.57E-05	1.99	60×60	2.60E-02	6.58E-05	1.91

Table 2: Numerical convergence results for the steady vortex in equilibrium. In the left table we report the results obtained on a quadrilateral mesh using the Osher type flux. For the results on the right we have employed a triangular mesh and the Rusanov type flux. The error refers to the difference between the computed water level h and the exact one at time $t_f = 0.5$.

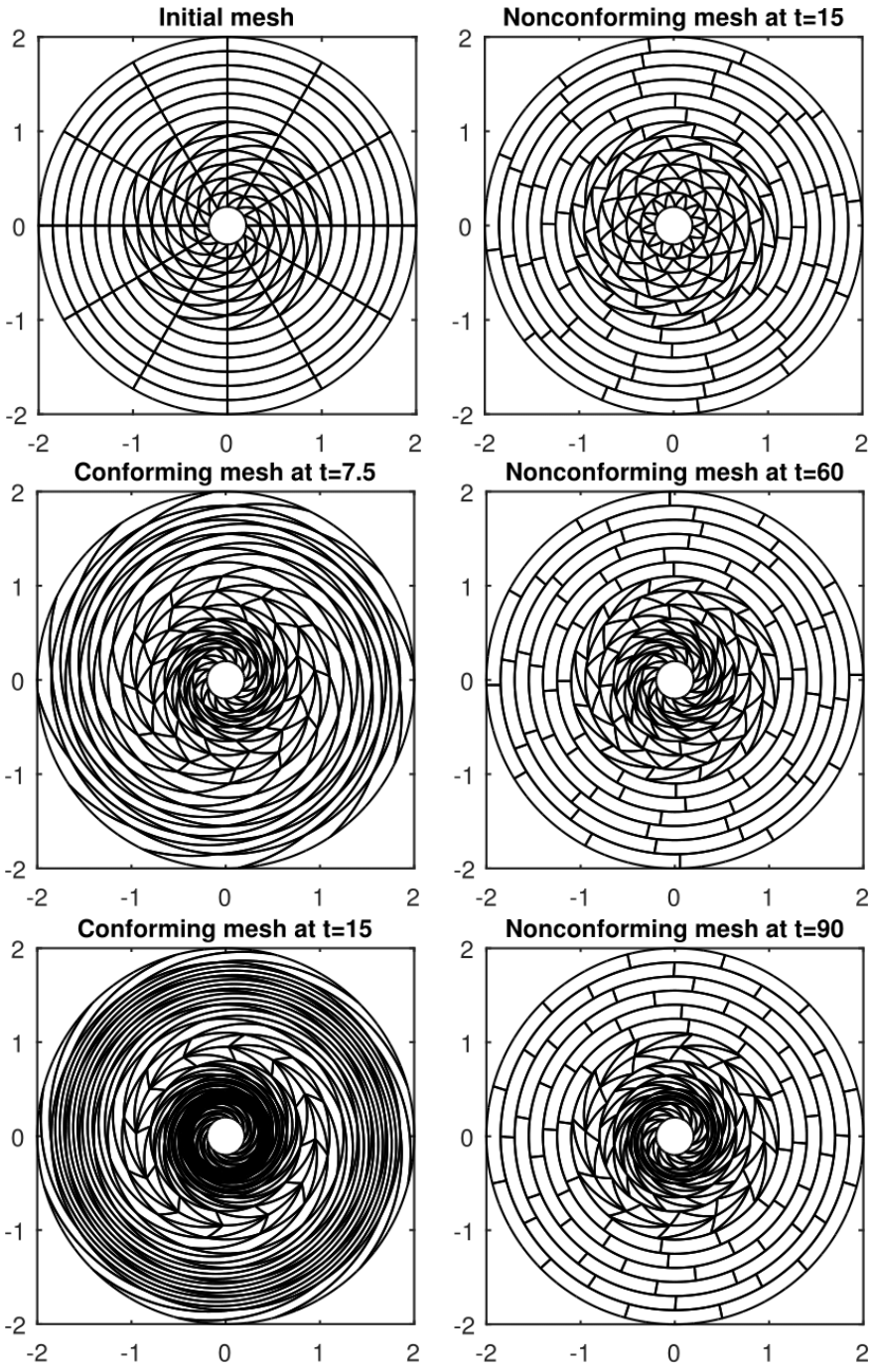

Figure 13: Steady vortex in equilibrium. We compared the behavior of a standard conforming algorithm (without any rezoning technique) and of our new nonconforming method. Using the conforming algorithm the elements are deformed in a very short time, the time step is heavily reduced and hence the computation is slower. On the contrary, the nonconforming slide lines introduced by our scheme are able to maintain a good shape of each element and an almost constant time step for a long computational time. Indeed only at time $t = 90$ some elements with $\rho \to 0$ are deformed because of the presence of shear *inside* the elements, which could be remedied only by subdividing the elements themselves.

$N_E \rightarrow$	216			264			300		
	conforming algorithm								
	t	n	Δt	t	n	Δt	t	n	Δt
	1	110	9.58E-03	1	180	5.40E-03	1	180	5.71E-03
	8	1163	4.13E-03	8	2180	2.52E-03	10	2071	3.11E-03
	12	2370	2.70E-03	12	4035	1.89E-03	15	4098	2.04E-03
stop at $\rightarrow$	15.3	**3773**	2.06E-03	15.5	**6072**	1.54E-03	17	5190	1.78E-03
	nonconforming algorithm								
	1	110	9.58E-03	1	180	5.82E-03	1	175	5.68E-03
	8	851	9.50E-03	8	1410	5.52E-03	10	1720	5.92E-03
	30	**3175**	9.30E-03	30	**6033**	4.06E-03	15	2565	5.94E-03
	60	7757	4.90E-03	60	15010	2.84E-03	80	15979	3.34E-03
stop at $\rightarrow$	119	26430	2.24E-03	129	35791	1.94E-03	132	36275	2.13E-03

Table 3: In this table we report the number of time steps n necessary to reach the time t and the dimension of the time step Δt at that time. We used three different meshes with N_E total number of elements (triangles or quadrilaterals). The results are obtained by applying a standard conforming method and our new nonconforming algorithm. Comparing the boxed numbers one can see that at the same time using the nonconforming method the Δt is more than the double w.r.t. the conforming method, even though at the beginning they were the same, and then looking at the bold data one can see that with almost the same number of time steps one reaches a simulation time that is twice as large. Besides the final simulation time that can be reached before obtaining an invalid mesh is almost 8 times larger.

results show that the method reaches its designed order of convergence and its overall accuracy. In particular, a high quality mesh is maintained and as a direct consequence the time step remains almost constant during the computation and the total amount of required computational effort is reduced, despite the increased algorithmic complexity of the numerical scheme on nonconforming meshes. Furthermore, despite the constraint of straight slip-lines, the proposed method is already able to deal with sufficiently complex situations that could be considered for practical applications, in particular in the astrophysical context (e.g. accretion discs and rotating gas clouds around stars, neutron stars or black holes).

The aim of our future research will be to remove the constraint of straight lines for the interface, adopting a distinction between master and slave nodes and improving the algorithms for the update of the connectivity tables. Moreover, we also plan to extend the presented method to better than second order of accuracy by extending the ADER-WENO ALE schemes [11, 9, 10] to moving nonconforming unstructured meshes. Furthermore, we also plan the incorporation of time accurate local time-steping (LTS) as forwarded in [31, 13, 39] into our algorithm in the future.

Acknowledgments

The research presented in this paper has been partially financed by the European Research Council (ERC) under the European Union's Seventh Framework Programme (FP7/2007-2013) with the research project *STiMulUs*, ERC Grant agreement no. 278267.

References

[1] D. Balsara. A two-dimensional hllc riemann solver for conservation laws: Application to euler and magnetohydrodynamic ows. *Journal of Computational Physics*, 231:7476–7503, 2012.

[2] D.S. Balsara. Multidimensional Riemann problem with self-similar internal structure Part I Application to hyperbolic conservation laws on structured meshes. *Journal of Computational Physics*, 277:163–200, 2014.
[3] D.S. Balsara and M. Dumbser. Multidimensional Riemann problem with self-similar internal structure Part II Application to hyperbolic conservation laws on unstructured meshes. *Journal of Computational Physics*, 287:269–292, 2015.
[4] A.J. Barlow and J. Whittle. Mesh adaptivity and material interface algorithms in a two dimensional Lagrangian hydrocode. *Chem Phys*, 19:15–26, 2000.
[5] T.J. Barth and D.C. Jespersen. The design and application of upwind schemes on unstructured meshes. *AIAA Paper 89-0366*, pages 1–12, 1989.
[6] M. Berndt, J. Breil, S. Galera, M. Kucharik, P.H. Maire, and M. Shashkov. Two–step hybrid conservative remapping for multimaterial arbitrary Lagrangian-Eulerian methods. *Journal of Computational Physics*, 230:6664–6687, 2011.
[7] P. Bochev, D. Ridzal, and M.J. Shashkov. Fast optimization-based conservative remap of scalar fields through aggregate mass transfer. *Journal of Computational Physics*, 246:37–57, 2013.
[8] W. Boscheri, D.S. Balsara, and M. Dumbser. Lagrangian ADER-WENO Finite Volume Schemes on Unstructured Triangular Meshes Based On Genuinely Multidimensional HLL Riemann Solvers. *Journal of Computational Physics*, 267:112–138, 2014.
[9] W. Boscheri and M. Dumbser. Arbitrary–Lagrangian–Eulerian One–Step WENO Finite Volume Schemes on Unstructured Triangular Meshes. *Communications in Computational Physics*, 14:1174–1206, 2013.
[10] W. Boscheri and M. Dumbser. A direct Arbitrary-Lagrangian-Eulerian ADER-WENO finite volume scheme on unstructured tetrahedral meshes for conservative and non-conservative hyperbolic systems in 3d. *Journal of Computational Physics*, 275:484 – 523, 2014.
[11] W. Boscheri, M. Dumbser, and D.S. Balsara. High-order ADER-WENO ALE schemes on unstructured triangular meshesapplication of several node solvers to hydrodynamics and magnetohydrodynamics. *Journal of Computational Physics*, 76:737–778, 2014.
[12] W. Boscheri, M. Dumbser, and D.S. Balsara. High Order Lagrangian ADER-WENO Schemes on Unstructured Meshes – Application of Several Node Solvers to Hydrodynamics and Magnetohydrodynamics. *International Journal for Numerical Methods in Fluids*, 76:737–778, 2014.
[13] W. Boscheri, M. Dumbser, and O. Zanotti. High Order Cell-Centered Lagrangian-Type Finite Volume Schemes with Time-Accurate Local Time Stepping on Unstructured Triangular Meshes. *Journal of Computational Physics*, 291:120–150, 2015.
[14] J. Breil, T. Harribey, P.H. Maire, and M. Shashkov. A multi-material ReALE method with MOF interface reconstruction. *Computers and Fluids*, 83:115–125, 2013.
[15] E.J. Caramana. The implementation of slide lines as a combined force and velocity boundary condition. *J Comput Phys*, 228:3911–3916, 2009.
[16] E.J. Caramana, D.E. Burton, M.J. Shashkov, and P.P. Whalen. The construction of compatible hydrodynamics algorithms utilizing conservation of total energy. *Journal of Computational Physics*, 146:227–262, 1998.
[17] E.J. Caramana and M.J. Shashkov. Elimination of artificial grid distorsion and hourglasstype motions by means of lagrangian subzonal masses and pressures. *Journal of Computational Physics*, 142:521–561, 1998.
[18] G. Carré, S. Del Pino, B. Després, and E. Labourasse. A cell-centered Lagrangian hydrodynamics scheme on general unstructured meshes in arbitrary dimension. *Journal of Computational Physics*, 228:5160–5183, 2009.
[19] M.R.J. Charesty, J. Bakosi, T.R. Canfield, A.R. Long, N.R. Morgan, J.Waltz, and J.G.Wohlbier. A High-Order Central ENO Method for ALE Simulation of Three-Dimensional Compressible Flows. *MULTIMAT 2015, Wurzburg*, 2015.
[20] J. Cheng and C.W. Shu. A high order ENO conservative Lagrangian type scheme for the compressible Euler equations. *Journal of Computational Physics*, 227:1567–1596, 2007.
[21] J. Cheng and C.W. Shu. A cell-centered Lagrangian scheme with the preservation of symmetry and conservation properties for compressible fluid flows in two-dimensional cylindrical geometry. *Journal of Computational Physics*, 229:7191–7206, 2010.
[22] J. Cheng and E.F. Toro. A 1D conservative Lagrangian ADER scheme. *Chinese Journal of Computational Physics*, 30:501–508, 2013.
[23] G. Clair, B. Despres, and E. Labourasse. A new method to introduce constraints in cell-centered Lagrangian schemes. *Computer Methods in Applied Mechanics and Engineering*, 261-262:56–65, 2013.
[24] G. Clair, B. Despres, and E. Labourasse. A one-mesh method for the cell-centered discretization of sliding. *Computer Methods in Applied Mechanics and Engineering*, 269:315–333, 2014.
[25] B. Després and C. Mazeran. Symmetrization of Lagrangian gas dynamic in dimension two and multimdimensional solvers. *C.R. Mecanique*, 331:475–480, 2003.
[26] B. Després and C. Mazeran. Lagrangian gas dynamics in two-dimensions and Lagrangian systems. *Archive for Rational Mechanics and Analysis*, 178:327–372, 2005.
[27] V.A. Dobrev, T.E. Ellis, Tz.V. Kolev, and R.N. Rieben. Curvilinear Finite elements for Lagrangian hydrodynamics. *International Journal for Numerical Methods in Fluids*, 65:1295–1310, 2011.
[28] V.A. Dobrev, T.E. Ellis, Tz.V. Kolev, and R.N. Rieben. High Order Curvilinear Finite Elements for Lagrangian Hydrodynamics. *SIAM Journal on Scientific Computing*, 34:606–641, 2012.
[29] V.A. Dobrev, T.E. Ellis, Tz.V. Kolev, and R.N. Rieben. High Order Curvilinear Finite Elements for axisymmetric Lagrangian Hydrodynamics. *Computers and Fluids*, 83:58–69, 2013.
[30] M. Dumbser D.S. Balsara and R. Abgrall. Multidimensional HLLC Riemann Solver for Unstructured Meshes - With Application to Euler and MHD Flows. *Journal of Computational Physics*, 261:172–208, 2014.
[31] M. Dumbser. Arbitrary–Lagrangian–Eulerian ADER–WENO finite volume schemes with time–accurate local time stepping for

hyperbolic conservation laws. *Computer Methods in Applied Mechanics and Engineering*, 280:57–83, 2014.
[32] M. Dumbser and E. F. Toro. On universal Osher–type schemes for general nonlinear hyperbolic conservation laws. *Communications in Computational Physics*, 10:635–671, 2011.
[33] M. Dumbser, A. Uuriintsetseg, and O. Zanotti. On Arbitrary–Lagrangian–Eulerian One–Step WENO Schemes for Stiff Hyperbolic Balance Laws. *Communications in Computational Physics*, 14:301–327, 2013.
[34] F.Vilar. Cell-centered discontinuous Galerkin discretization for two-dimensional Lagrangian hydrodynamics. *Computers and Fluids*, 64:64–73, 2012.
[35] F.Vilar, P.H. Maire, and R. Abgrall. Cell-centered discontinuous Galerkin discretizations for two-dimensional scalar conservation laws on unstructured grids and for one-dimensional Lagrangian hydrodynamics. *Computers and Fluids*, 46(1):498–604, 2010.
[36] F.Vilar, P.H. Maire, and R. Abgrall. A discontinuous Galerkin discretization for solving the two-dimensional gas dynamics equations written under total Lagrangian formulation on general unstructured grids. *INRIA Research Report No 8483 2014*, 2014. available at http://hal.inria.fr/docs/00/95/07/82/PDF/RR-8483.pdf.
[37] S.K. Godunov. Finite difference methods for the computation of discontinuous solutions of the equations of fluid dynamics. *Mathematics of the USSR: Sbornik*, 47:271–306, 1959.
[38] S.K. Godunov, A. Zabrodine, M. Ivanov, A. Kraiko, and G. Prokopov. Rèsolution numèrique desproblémes multidimensionnels de la dynamique des gaz. *Mir*, 1979.
[39] D. da Motta-Marques J.R. Cavalcanti, M. Dumbser and C.R. Fragoso Junior. A Conservative Finite Volume Scheme with Time-Accurate Local Time Stepping for Scalar Transport on Unstructured Grids. *Advances in Water Resources*, 86:217–230, 2015.
[40] M. Kucharik, R. Liska, J. Limpouch, and P. Vchal. ALE simulations of high-velocity impact problem. *Journal of Computational Physics*, 76:737–778, 2014.
[41] M. Kucharik and M.J. Shashkov. One-step hybrid remapping algorithm for multi-material arbitrary Lagrangian-Eulerian methods. *Journal of Computational Physics*, 231:2851–2864, 2012.
[42] M. Kuchark, R. Loubére, L. Bednàrik, and R. Liska. Enhancement of Lagrangian slide lines as a combined force and velocity boundary condition. *Computers & Fluids*, 83:3–14, 2013.
[43] Z. Li, X. Yu, and Z. Jia. The cell–centered discontinuous Galerkin method for Lagrangian compressible Euler equations in two dimensions. *Computers and Fluids*, 96:152–164, 2014.
[44] W. Liu, J. Cheng, and C.W. Shu. High order conservative Lagrangian schemes with LaxWendroff type time discretization for the compressible Euler equations. *Journal of Computational Physics*, 228:8872–8891, 2009.
[45] R. Loubére, M. Dumbser, and S. Diot. A new family of high order unstructured MOOD and ADER finite volume schemes for multidimensional systems of hyperbolic conservation law. *Communications in Computational Physics*, 16:718–763, 2014.
[46] R. Loubère, P.H. Maire, and P. Váchal. A second-order compatible staggered Lagrangian hydrodynamics scheme using a cell-centered multidimensional approximate Riemann solver. *Procedia Computer Science*, 1:1931–1939, 2010.
[47] R. Loubère, P.H. Maire, and P. Váchal. 3D staggered Lagrangian hydrodynamics scheme with cell-centered Riemann solver-based artificial viscosity. *International Journal for Numerical Methods in Fluids*, 72:22–42, 2013.
[48] R. Loubére, S.Diot, and M.Kucharik. High order remapping method using MOOD paradigm. *MULTIMAT 2013, San Francisco*, 2013.
[49] R. Loubère and M.J. Shashkov. A subcell remapping method on staggered polygonal grids for arbitrary–lagrangian–eulerian methods. *Journal of Computational Physics*, 23:155–160, 2004.
[50] P.H. Maire. A high-order cell-centered lagrangian scheme for two-dimensional compressible fluid flows on unstructured meshes. *Journal of Computational Physics*, 228:2391–2425, 2009.
[51] P.H. Maire. A high-order one-step sub-cell force-based discretization for cell-centered lagrangian hydrodynamics on polygonal grids. *Computers and Fluids*, 46(1):341–347, 2011.
[52] P.H. Maire. A unified sub-cell force-based discretization for cell-centered lagrangian hydrodynamics on polygonal grids. *International Journal for Numerical Methods in Fluids*, 65:1281–1294, 2011.
[53] P.H. Maire, R. Abgrall, J. Breil, and J. Ovadia. A cell-centered lagrangian scheme for two-dimensional compressible flow problems. *SIAM Journal on Scientific Computing*, 29:1781–1824, 2007.
[54] C.D. Munz. On Godunov–type schemes for Lagrangian gas dynamics. *SIAM Journal on Numerical Analysis*, 31:17–42, 1994.
[55] A. López Ortega and G. Scovazzi. A geometrically–conservative, synchronized, flux–corrected remap for arbitrary Lagrangian–Eulerian computations with nodal finite elements. *Journal of Computational Physics*, 230:6709–6741, 2011.
[56] G. Scovazzi. Lagrangian shock hydrodynamics on tetrahedral meshes: A stable and accurate variational multiscale approach. *Journal of Computational Physics*, 231:8029–8069, 2012.
[57] E.F. Toro. *Riemann Solvers and Numerical Methods for Fluid Dynamics*. Springer, second edition, 1999.
[58] B. van Leer. Towards the ultimate conservative difference scheme II: Monotonicity and conservation combined in a second order scheme. *Journal of Computational Physics*, 14:361–370, 1974.
[59] J. von Neumann and R.D. Richtmyer. A method for the calculation of hydrodynamics shocks. *Journal of Applied Physics*, 21:232–237, 1950.
[60] M. L. Wilkins. Calculation of elastic-plastic flow. *Methods in Computational Physics*, 3, 1964.
[61] Y.V. Yanilkin, E.A. Goncharov, V.Y. Kolobyanin, V.V. Sadchikov, J.R. Kamm, M.J. Shashkov, and W.J. Rider. Multi-material pressure relaxation methods for lagrangian hydrodynamics. *Computers and Fluids*, 83:137–143, 2013.